

Accelerated Article Preview**Cells of the adult human heart**

Received: 10 February 2020

Accepted: 18 September 2020

Accelerated Article Preview Published
online 24 September 2020

Cite this article as: Litviňuková, M. et al.
Cells of the adult human heart. *Nature*
<https://doi.org/10.1038/s41586-020-2797-4>
(2020).

Open access

Monika Litviňuková, Carlos Talavera-López, Henrike Maatz, Daniel Reichart, Catherine L. Worth, Eric L. Lindberg, Masatoshi Kanda, Krzysztof Polanski, Matthias Heinig, Michael Lee, Emily R. Nadelmann, Kenny Roberts, Liz Tuck, Eirini S. Fasouli, Daniel M. DeLaughter, Barbara McDonough, Hiroko Wakimoto, Joshua M. Gorham, Sara Samari, Krishnaa T. Mahbubani, Kourosh Saeb-Parsy, Giannino Patone, Joseph J. Boyle, Hongbo Zhang, Hao Zhang, Anissa Viveiros, Gavin Y. Oudit, Omer Bayraktar, J. G. Seidman, Christine E. Seidman, Michela Nosedá, Norbert Hubner & Sarah A. Teichmann

This is a PDF file of a peer-reviewed paper that has been accepted for publication. Although unedited, the content has been subjected to preliminary formatting. Nature is providing this early version of the typeset paper as a service to our authors and readers. The text and figures will undergo copyediting and a proof review before the paper is published in its final form. Please note that during the production process errors may be discovered which could affect the content, and all legal disclaimers apply.

Cells of the adult human heart

<https://doi.org/10.1038/s41586-020-2797-4>

Received: 10 February 2020

Accepted: 18 September 2020

Published online: 24 September 2020

Open access

Monika Litviňuková^{1,2,21}, Carlos Talavera-López^{1,3,21}, Henrike Maatz^{2,21}, Daniel Reichart^{4,6,21}, Catherine L. Worth², Eric L. Lindberg², Masatoshi Kanda^{2,20}, Krzysztof Polanski¹, Matthias Heinig^{15,16}, Michael Lee⁷, Emily R. Nadelmann⁴, Kenny Roberts¹, Liz Tuck¹, Eirini S. Fasouli¹, Daniel M. DeLaughter⁴, Barbara McDonough^{12,13}, Hiroko Wakimoto⁴, Joshua M. Gorham⁴, Sara Samari⁷, Krishnaa T. Mahbubani⁹, Kourosh Saeb-Parsy⁹, Giannino Patone², Joseph J. Boyle⁷, Hongbo Zhang^{1,19}, Hao Zhang^{17,18}, Anissa Viveiros^{17,18}, Gavin Y. Oudit^{17,18}, Omer Bayraktar¹, J. G. Seidman^{4,22}, Christine E. Seidman^{4,13,14,22}, Michela Nosedà^{7,8,22}, Norbert Hubner^{2,10,11,12,22} & Sarah A. Teichmann^{1,5,22}

Cardiovascular disease is the leading cause of death worldwide. Advanced insights into disease mechanisms and therapeutic strategies require deeper understanding of the healthy heart's molecular processes. Knowledge of the full repertoire of cardiac cells and their gene expression profiles is a fundamental first step in this endeavor. Here, using state-of-the-art analyses of large-scale single-cell and nuclei transcriptomes, we characterise six anatomical adult heart regions. Our results highlight the cellular heterogeneity of cardiomyocytes, pericytes, and fibroblasts, revealing distinct atrial and ventricular subsets with diverse developmental origins and specialized properties. We define the complexity of the cardiac vasculature and its changes along the arterio-venous axis. In the immune compartment we identify cardiac resident macrophages with inflammatory and protective transcriptional signatures. Further, inference of cell-cell interactions highlight different macrophage-fibroblast-cardiomyocyte networks between atria and ventricles that are distinct from skeletal muscle. Our human cardiac cell atlas improves our understanding of the human heart and provides a healthy reference for future studies.

The heart is a complex organ, composed of four morphologically and functionally distinct chambers (Figure 1a). Deoxygenated blood from the low pressure right atrium and ventricle is propelled into the lungs. Oxygenated blood enters the left atrium and ventricle, which propels blood across the body at systemic pressure. Chambers are separated by the interatrial and interventricular septa and unidirectional flow is established by the atrio-ventricular and ventricular-arterial valves. An intrinsic electrophysiologic system rapidly propagates electrical impulses from the sinoatrial node to the atrioventricular node, and along Purkinje fibers to the apex where contraction begins. Cardiac anatomical and functional complexity requires exquisite orchestration of heterogeneous cell populations to enable continuous contraction and relaxation across different pressures, strains, and biophysical stimuli in each chamber.

The heart is derived from multipotent progenitor cells comprising two heart fields. Cells of the first heart field primarily populate the

left ventricle; second heart field cells populate the right ventricle, and both fields contribute to atria. The distinct gene regulatory networks operating in each heart field and postnatal hemodynamics, presumably prime gene expression patterns of adult heart cells¹.

Single-cell and single-nucleus transcriptomics (scRNA-Seq, snRNA-Seq) and multiplex smFISH enable the identification of anatomical specificities, molecular signatures, intercellular networks and spatial relationships by illuminating the coordinated communication of cardiac cells within their microenvironments².

We present comprehensive transcriptomic data on six distinct cardiac regions, providing the largest reference framework to date^{3,4}. We incorporate snRNA-Seq to ensure high throughput capture of large cardiomyocytes (length/width: ~100/25 μm) and scRNA-Seq to upsample and enrich endothelial and immune cell populations. Using multiplex smFISH imaging, we describe the spatial distribution of selected cell populations and cell-cell co-localisations. We compare cardiac cell

¹Cellular Genetics Programme, Wellcome Sanger Institute, Wellcome Genome Campus, Hinxton, Cambridge, CB10 1SA, United Kingdom. ²Cardiovascular and Metabolic Sciences, Max Delbrück Center for Molecular Medicine in the Helmholtz Association (MDC), Berlin, Germany. ³EMBL - EBI, Wellcome Genome Campus, Hinxton, Cambridge, CB10 1SA, United Kingdom. ⁴Department of Genetics, Harvard Medical School, Boston, MA, United States. ⁵Dept Physics/Cavendish Laboratory, University of Cambridge, JJ Thompson Ave, Cambridge, CB3 0EH, United Kingdom. ⁶Department of Cardiology, University Heart & Vascular Center, University of Hamburg, Hamburg, Germany. ⁷National Heart and Lung Institute, Imperial College London, London, United Kingdom. ⁸British Heart Foundation Centre of Research Excellence and Centre of Regenerative Medicine, Imperial College London, London, United Kingdom. ⁹Department of Surgery, University of Cambridge, NIHR Cambridge Biomedical Centre, and Cambridge Biorepository for Translational Medicine, Cambridge, United Kingdom. ¹⁰Charité - Universitätsmedizin, Berlin, Germany. ¹¹Berlin Institute of Health (BIH), Berlin, Germany. ¹²DZHK (German Centre for Cardiovascular Research), Partner Site Berlin, Berlin, Germany. ¹³Cardiovascular Division, Brigham and Women's Hospital, Boston, MA, United States. ¹⁴Howard Hughes Medical Institute, Chevy Chase, MD, United States. ¹⁵Institute of Computational Biology (ICB), HMGU, Neuherberg, Germany. ¹⁶Department of Informatics, Technische Universität München (TUM), Munich, Germany. ¹⁷Division of Cardiology, Department of Medicine, Faculty of Medicine and Dentistry, University of Alberta, Edmonton, Canada. ¹⁸Mazankowski Alberta Heart Institute, Faculty of Medicine and Dentistry, University of Alberta, Edmonton, Canada. ¹⁹Department of Histology and Embryology of Zhongshan School of Medicine, Sun-Yat Sen University, Guangzhou, China. ²⁰Department of Rheumatology and Clinical Immunology, Sapporo Medical University, Sapporo, Japan. ²¹These authors contributed equally: Monika Litviňuková, Carlos Talavera-López, Henrike Maatz, Daniel Reichart. ²²These authors jointly supervised this work: J. G. Seidman, Christine E. Seidman, Michela Nosedà, Norbert Hubner, Sarah A. Teichmann. [✉]e-mail: seidman@genetics.med.harvard.edu; cseidman@genetics.med.harvard.edu; m.nosedà@imperial.ac.uk; nhueber@mdc-berlin.de; st9@sanger.ac.uk

and nuclear transcriptomes with those of skeletal muscle and kidney, highlighting cardiac-specific cell signatures. Our study defines the cellular and molecular signatures of the adult healthy heart enabling functional plasticity in response to varying physiological conditions and disease.

Adult human heart cellular landscape

We isolate single cells, nuclei and CD45+ enriched cells from the left/right ventricular free walls, left/right atrium, (denoted LV, RV, LA, RA), the LV apex (AX), and interventricular septum (SP), from fourteen adults (Figure 1a, b, Supplementary Table 1). After processing with 10X Genomics and a generative deep variational autoencoder, the resulting dataset comprises 45,870 cells, 78,023 CD45+ enriched cells and 363,213 nuclei for 11 major cell types: atrial cardiomyocytes (aCM), ventricular cardiomyocytes (vCM), fibroblasts (FB), endothelial cells (EC), pericytes (PC), smooth muscle cells (SMC), immune (myeloid, Myel; lymphoid, Lym), adipocytes (Adip), mesothelial cells (Meso) and neuronal cells (NC) (Figure 1c, e, Extended Data Figure 1 and 2).

The distributions of these main cell types, estimated from nuclei data, differ between atrial and ventricular tissues. Atrial tissues contain 30.1% CM, 24.3% FB, 17.1% mural cells (PC and SMC), 12.2% EC and 10.4% immune cells (Myel and Lym). In contrast, ventricular regions (AX, SP, LV, RV) contain 49.2% vCM, 21.2% mural cells, 15.5% FB, 7.8% EC and 5.3% immune cells (Figure 1d, Supplementary Table 2).

The ventricular proportions of vCM and FB are negatively correlated, while PC and SMC proportions are positively correlated, implying a functional organization (Supplementary Table 3). Cell distributions are generally similar in male and female hearts. However, the mean percentages of vCM from LV and RV are higher in females ($56 \pm 9\%$) and associated with a stronger negative correlation between vCM and FB ($r = -0.8$; slope = -0.9) compared to male hearts ($47 \pm 11\%$; p -value = 0.03 ; vCM:FB, $r = -0.4$; slope = -0.3). Differences in CM proportions is unexpected given the average smaller female heart mass, and if confirmed might explain higher cardiac stroke volumes in women⁵ and lower rates of cardiovascular disease.

Cardiomyocyte heterogeneity

CM show high-level expression of genes encoding contractile force generating sarcomere proteins (*TTN*, *MYBPC3*, *TNNT2*) and for calcium-mediated processes (*RYR2*, *PLN*, *SLC8A1*). Consistent with bulk tissue RNAseq data⁶, we observe strikingly distinct transcriptional signatures in vCM and aCM reflecting developmental origins and differences in electrophysiological, contractile, and secretory processes (Extended Data Figure 3, Supplementary Table 4).

vCM are enriched in genes encoding sarcomere proteins (*MYH7*, *MYL2*), transcription factors (*IRX3*, *IRX5*, *IRX6*, *MASPL1*, *HEY2*), and *PRDM16*, mutated in LV non-compaction⁷. Other abundant transcripts enable tissue integrity despite high ventricular strain: *PCDH7* encodes a calcium-dependent strong adhesive molecule⁸; *SMYD2* encodes a lysine methyltransferase promoting sarcomere formation and stabilization⁹. aCM abundantly express prototypic genes and also *ALDH1A2*, an enzyme required for retinoic acid synthesis, *ROR2*, participating in Wnt-signaling during lineage differentiation¹⁰, and *SYNPR*, functioning in TRP-channel mechanosensing by atrial volume receptors¹¹

We identify five vCM populations: vCM1 comprise 63.9% of LV but only 36.7% of RV cardiomyocytes (Figure 2a, b, Extended Data Figure 3a, c-e, Supplementary Table 5, 6). vCM2 is more RV enriched (39.9%) compared to LV (9.1%). However, differences between vCM1 and vCM2 are small, implying shared LV (enriched in vCM1) and RV (enriched in vCM2) gene programs. vCM2 shows higher expression of *PRELID2*, a developmental molecule with unknown cardiac function¹² (verified by smFISH, Figure 2c, Extended Data Figure 3c). Among vCMs, vCM2 has the highest expression of *MYH6* and *CDH13*, a cell surface T-cadherin

receptor for cardioprotective adiponectin and low density lipoproteins, both associated with multiple cardiometabolic traits¹³.

vCM3 and vCM4 are present across all ventricular regions. The vCM3 transcriptional profile resembles a prominent RA population (aCM3, discussed below) with retinoic acid-responsive SMC gene enrichment (*MYH9*, *NEXN*, *CNN1*)^{14,15}. vCM3 also express stress-response genes including *ANKRD16*, *FHL1*¹⁷ (verified by smFISH, Figure 2d, Extended Data Figure 3c), *DUSP27*¹⁸, and *XIRP1/XIRP2*, interacting with intercalated disc ion channel proteins implicated in cardiomyopathy and arrhythmias¹⁹. The small population vCM4 is enriched for nuclear-encoded mitochondrial genes (*NDUFB11*, *NDUFA4*, *COX7C*, *COX5B*) and Gene Ontology terms indicative of a high energetic state (Extended Data Figure 3f). vCM4 also demonstrates high levels of *CRYAB*, encoding a cytoprotective and antioxidant heat shock protein²⁰, of sarcomere protein genes and *PLN*, implying these vCM are outfitted to perform higher workload than other vCM.

vCM5 (-1%) comprises cells with high levels of *DLCL1* and *EBF2*²¹, regulating brown adipocyte differentiation and perhaps cardiac pacemaker activity, and transcripts identified in neuronal lineages (*SOX5*, *EBF1*, *KCNAB1*). As *EBF1*-depleted mice have a profoundly hypoplastic ventricular conduction system²², vCM5 may participate in electrophysiology.

We identify five aCM populations (Figure 2e, f, Extended Data Figure 3b-d, Supplementary Table 6, 7). *HAMP*, a master regulator of iron homeostasis, is significantly enriched in over 50% of RA CM vs. 3% LA CM (verified by smFISH, Figure 2g, Extended Data Figure 3c)²³, implying energetic differences⁶. *HAMP* has unknown roles in cardiac biology, but *Hamp*-null mice have electron transport chain deficits and lethal cardiomyopathy²⁴.

aCM1 shows robust expression of prototypic atrial transcripts, indicative of basal aCM gene program, and lower levels of molecules with neuronal functions (*ADGRL2*, *NFXL1*, *ROBO2*). aCM2 predominantly expresses *HAMP* within the RA and is enriched for *SLIT3*, the developmental ligand for cardiac ROBO receptors²⁵, *ALDH1A2*²⁶ and *BRINP3*, involved in retinoic acid signaling, and *GRXCR2*, supporting cilia involved in mechanosensing²⁷.

aCM3 and vCM3 share similar transcriptional profiles including SMC gene *CNN1* enrichment (verified by smFISH, Figure 2h, Extended Data Figure 3c). The molecular signatures of aCM2, aCM3 and vCM3 imply derivation from the second heart field²⁸. aCM4 transcripts denote high metabolic activity, similar to vCM4, and have the highest *NPPA* expression. aCM5 express transcripts similar to vCM5.

Vascular, stromal and mesothelial cells

The vascular compartment includes 17 distinct populations of EC, SMC, PC, mesothelial cells with anatomical and arterio-venous specificities (Figure 3a, b, Supplementary Table 8, 9). Endothelial cells, identified by pan-EC markers *PECAMI1*, *CDH5* and *VWF*, comprise ten populations (Extended Data Figure 4a-c, g). Three capillary EC (EC1-3_cap), expressing *RGCC* and *CA4*²⁹, represent 57.4% of all EC. Capillary-like EC4_immune express antigen-presentation and immune-regulation related transcripts (*CX3CLI*, *CCL2*, *IL6* and *ICAM1*)³⁰. Arterial EC5_art is enriched for *SEMA3G*, *EFNB2*, *DLL4*, while EC6_ven express venous marker *NR2F3*³¹ and *ACKR1*³², which we confirm by smFISH (Figure 3c). Mainly atrial EC7_atria express *SMOCL1*, an angiogenesis regulator³³ and *NPR3*, detected in mouse endocardium³⁴ suggestive for endocardial cells. Lymphatic EC8_In, enriching for *PROX1*, *TBX1* and *PDPN*, represent -1% of the captured EC²⁹.

Pericytes express *ABCC9* and *KCNJ8* and segregate into four clusters, with PC1_vent enriched in ventricles and PC2_atria in atria. PC1_vent express adhesion molecules (*NCAM2*, *CD38*), and *CSPG4*, involved in microvascular morphogenesis and EC cross-talk³⁵ (Extended Data Figure 4d-f). PC3_str co-express PC markers and very low levels of pan-EC transcripts. RNA velocity analyses suggest a directionality that implies PC3_str as a transitional state between PC and EC (Extended Data

Figure 4h,i). These observations may relate to bidirectional pericyte/endothelial cell (trans)differentiation, which remains controversial³⁶.

Vascular SMC expressing *MYH11* split into two populations. SMC1_{basic} express transcripts indicating immaturity, including stem cell marker *LGR6*³⁷ and proliferation associated *RGS5*³⁸. SMC2_{art} shows significantly higher levels of *CNN1*, *ACTA2* and *TAGLN*, implying arterial origin while SMC1_{basic}, are possibly venous-derived³⁹ (Extended Data Figure 4d-f).

Cell-cell interaction analyses infer connections between EC and mural cells in different vascular segments (Figure 3b-d, Extended Data Figure 4j,k, Supplementary Table 10) including Notch receptors-ligands interactions⁴⁰ (NOTCH1/NOTCH4 with JAG1 and NOTCH2/NOTCH3 with JAG1/JAG2/DLL4) between EC5_{art} with SMC2_{art}. Exploratory spatial transcriptomics (Extended Data Figure 5) shows co-occurrence of EC5_{art} and SMC2_{art} markers and *JAG1*, *NOTCH2* supporting this interaction. A venous-specific DLL1-NOTCH3 interaction is predicted for EC6_{ven} and SMC1_{basic}. Notably, many of the venous and arterial EC predicted interactions are shared with capillary EC, suggesting gradual changes along the arterio-venous axis³⁹.

We define a distinct small population as mesothelial cells (Meso) enriching for *MSLN*, *WT1*, and *BNC1*⁴¹ while lacking EC, FB or mural genes. smFISH confirms this annotation with localisation of BNC1+/CDH5- cells to the epicardium (Extended Data Figure 4l-n).

Cardiac fibroblast cells

Cells of the FB compartment show enriched expression of *DCN*, *GSN* and *PDGFRA* within seven populations (Figure 3g) with regional enrichment in ventricles (FB1) and atria (FB2). This is consistent with distinctive functional properties, including stronger profibrotic responses, by atrial FB⁴². FB1 and FB2, express canonical genes and define a basal, chamber-specific FB expression programme (Extended Data Figure 6a, Supplementary Table 11).

FB4 and FB5 are less abundant in the RA compared to other regions, while FB3 are less in the left ventricle (Extended Data Figure 6c). FB4 express genes responsive to TGF- β signaling (e.g. *POSTN* and *TNC*) (Figure 3e). FB5 has higher expression of genes involved in extracellular matrix (ECM) production, remodeling, and degradation. In contrast, FB3 has lower expression of ECM-related genes but higher expression of cytokine receptors like *OSMR* and *ILST6* (Figure 3f, Extended Data Figure 6b, Supplementary Table 12)⁴³. These distinctive fibroblasts' gene programs likely govern stress-responsive cardiac remodeling and contribute to homeostasis.

Separate clustering of atrial and ventricular FB recapitulated the populations described above, including an OSM-signalling population in each chamber (aFB4, vFB3). Additionally, we identify distinct chamber-specific ECM-producing FB differing in the expression of collagen isoforms and other ECM- (aFB2 vs. vFB2) (Extended Data Figure 6g-m, Supplementary Table 13) or connective tissue-related genes (aFB1 vs. vFB4).

Immune cells and cardiac homeostasis

Analysis of cardiac immune cells reveals 21 cell states (Figure 4a and Extended Data Figure 7). Myeloid cells comprise 13 populations, including multiple M Φ , monocytes (Mo) and dendritic cell subtypes, whereas the lymphoid compartment comprises 8 populations (Supplementary Tables 14, 15).

M Φ include three *LYVE1*+M Φ populations: *LYVE1*+M Φ 1-2 enrich for clathrin and cathepsin genes and *LYVE1*+M Φ 3 for *HLA-DOA*, *HLA-DQA1-2*, *HLA-DQB1*. *LYVE1*+M Φ appear related to recently described tissue-resident M Φ associated with cardiovascular remodeling⁴⁴, although *TIMD4*⁴⁵ (Extended Data Figure 8a,b). Monocyte-derived M Φ s (M Φ _mod) express *LYVE1* and *FOLR2*, Mo-like markers *CEBPA* and *S100A8*, and chemoattractant cytokine genes *CCL13* and *CCL18*. Antigen-presenting M Φ (M Φ _AgP) are *FOLR2*-, *LYVE1*-, *MERTK*- and enrich

for *HLA-DRA*, *HLA-DMA*, *HLA-DMB* and *HLA-DPA1* and *TREM2* (described in lipid-associated M Φ ;LAM)⁴⁶. While monocytes are abundant in our data and others⁴⁷, these are likely circulating, as supported by computational integration of our data with published BMC scRNAseq data (Supplementary Table 16). Two populations of *DOCK4*+M Φ differentiated by higher expression of *IL4R*, *STAT3* and *ITGA1* in *DOCK4*+M Φ 1 versus *DOCK4*+M Φ 2, do not express *CIQA* or *FOLR2* (Extended Data Figure 8c).

Predicted cell-cell interactions identify receptor-ligand circuits among immune cells, CM, and FB. *LYVE1*+M Φ , M Φ _mod and M Φ _AgP are predicted to interact with FB4 via CD74-MIF (Figure 4b, Extended Data Figure 8d,e and Supplementary Table 17). Inhibition of this interaction leads to fibrosis⁴⁸ and tissue damage⁴⁹. FB4 also enrich for *FNI*, *COL4A1* and *TNC*, facilitating cellular proliferation in the fetal heart⁵⁰ and predicted to interact with different integrins in aCM and vCM. In SKM, predicted cell-cell interactions between *PRG4*+FB (analogous to FB4) and myocytes involve *COL1A2*, *COL6A2* and α 10b1 integrins, while SKM FB and Mo appear to interact *via* the CXCR4-CXCL12 chemokine pair (Figure 4b, Supplementary table 18), implying tissue-specific homeostatic transcriptional circuits.

Using a logistic regression model, we find that lymphoid cells are more similar across heart, SKM and kidney, while there is less concordance for myeloid cells (Extended Data Figure 8f, Supplementary Table 16,19), probably due to tissue-specific adaptability of myeloid cells⁵¹. Notably, populations corresponding to cardiac M Φ _mod, *LYVE1*+M Φ 1, *DOCK4*+M Φ 1-2 and M Φ _AgP are absent from the SKM and kidney. Cardiac *LYVE1*+M Φ 2-3, pro-inflammatory monocytes (Mo_pi), classical monocytes (Mo_classic) and Mast cells are more similar to their SKM counterparts, indicating greater similarity of striated muscle and cardiac myeloid populations versus kidney. The transcriptional signature of cardiac *LYVE1*+M Φ 2-3 is specific without overlap in SKM and kidney (Figure 4c).

Conduction System and Neuronal Cells

Among 3,961 cells expressing prototypic electrophysiologic transcripts (*NRXN1*, *NRXN3*, *KCNMB4*), we identify six NC subclusters (Extended Data Figure 9a-c). NC1 constitutes 75-80% of NC and exhibits a basal gene program including *LGI4*, required for glia development and axon myelination⁵². NC2 and NC4 show strong expression of the central nervous system marker, *PRKG1*⁵³, and co-express typical fibroblasts and CM genes, respectively. NC3 has overlapping gene expression signatures with EC. NC5 expresses *LGR5*, a Wnt-signaling, G-protein-coupled receptor and stem cell marker that promotes CM differentiation in the outflow tract⁵⁴, an arrhythmogenic area⁵⁵. This cluster also expresses the neurodegenerative disease gene, *PPP2R2B*⁵⁶ (verified by smFISH, Extended Data Figure 9d, Supplementary Table 20), *LSAMP* which patterns neuronal connections⁵⁷, and *LPL* a lipoprotein transport enzyme that remyelinates damaged neurons⁵⁸. NC6 mimics Schwann cells, expressing *MBP*, *PRX*, and *MPZ*, encoding myelin constituents⁵⁹.

Adipocytes

Cardiac adipocytes uniformly express *GPAM*, *FASN*, *ADIPOQ* and at lower levels, *LEP*⁶⁰ (Extended Data Figure 9e-h). Adip1 expresses genes for PPAR-pathways, metabolism of lipids and lipoproteins, and lipolysis. Adip2, expresses ECM genes such as *LAMA2*, *IGFBP7*, and *FBNI*, which encodes both the glycoprotein fibrillin1 and asprosin, a white adipose tissue secreted hormone involved in glucose homeostasis (Supplementary Table 21). Given a stromal-related molecular signature, Adip2 cells may represent fibrogenic adipocytes and/or precursors^{61,62}. Adip3 transcripts encode inflammatory and cytokine responsive molecules.

COVID-19 and GWAS disease relevance

Transcripts encoding the SARS-CoV-2 receptor, *ACE2*⁶³ are highest in PC, followed by FB and lowest in CM where expression is 2-fold higher

in vCM than aCM. Among proteases priming viral entry⁶³, *TMPRSS2* transcripts are absent in PC, FB and CM, while *CTSB* and *CTSL* are lowly expressed with higher levels in CM. *ACE2* expression in pericytes and fibroblasts is depicted by smFISH (Extended Data Figure 10a-e).

We define cells enriched for genes from 12 cardiovascular GWAS studies and involved in SARS-CoV-2 infection using MAGMA⁶⁴ (Extended Data Figure 10f). Atrial fibrillation (AF) GWAS signals are associated with transcriptional profiles in vCM3, due to higher mean expression of *CAV1*, *CAV2*, and *PRRX1*. PR interval GWAS signals are associated with vCM3 and aCM5, with high expression of *SCNSA*, *CAV1*, *ARHGAP24*, *MEIS1*, *TBX5* and *TTN*. GWAS signals for QRS duration are associated with specific gene expression in NC2 (*PRKCA*, *CEP85L*, *SLC35F1*, *SIPA1L1*, *KLF12*, *FADS2*). Coronary artery disease and hypertension GWAS signals are associated with transcripts from many cell lineages, particularly SMC, FB, and EC, reflecting the relevance of vascular cells in both disorders.

Discussion

Our analyses of approximately half a million single cells and nuclei from six distinct cardiac regions from 14 donors significantly expand an emerging reference adult heart cell atlas. By combining sc/snRNA-Seq data with machine learning and *in situ* imaging techniques, we provide detailed insights across the repertoire of cardiac cells, including CM (excluded by scRNA-Seq) and EC (underrepresented in cardiac snRNA-Seq). We quantify the cellular composition highlighting chamber-specific features and differences between male and female donors. Within each cell compartment, we identify and validate prototypic lineage-specific genes, and genes with previously unknown cardiac expression. Our results begin to unravel the molecular underpinnings of cardiac physiology and the cellular response to stress and disease.

CM are the most prevalent cardiac cells and comprise higher percentages in ventricles than atria, and in female *versus* male ventricular tissues. Transcriptional differences between aCM and vCM populations indicate different developmental origins, distinctive hemodynamic forces and specialized functions in cardiac chambers. Cellular diversity of FB reveals ECM-producing and ECM-organising activities that with other cells support CM across varying biophysical stimuli. The vascular compartment contains multiple EC and PC populations and two SMC subtypes with distinct anatomical and arterio-vascular characteristics. Arterial and venous EC are predicted to interact with mural cells via Notch signaling pathways involved in regulating vascular homeostasis and development. Immune cells interact with FB and CM. In addition to confirming previous findings^{65,66}, we show macrophage complexity and infer paracrine circuits for cardiac homeostasis. Cross-tissue analyses delineate cardiac populations distinct from skeletal muscle and kidney.

We illustrate the relevance of cardiac cell atlas by defining cell lineages enriched in cardiovascular GWAS and molecules involved in SARS-CoV-2 infection. High expression of the viral receptor *ACE2* in pericytes and its correlation with *AGTR1* is consistent with the role of renin-angiotensin-aldosterone system (RAAS) signalling in cardiac hemodynamics⁶⁷.

We recognize limitations associated with cell capture by different data sources and unintended bias from surgical sampling. However, we expect our results will inform studies of other cardiac regions (valves, papillary muscle, conduction system), propel studies with large cohorts to elucidate the roles of age, gender, and ancestry on normal cardiac physiology and provide critical insights to enable mechanistic understanding of heart disease. All of our data can be explored at www.heartcellatlas.org.

Online content

Any methods, additional references, Nature Research reporting summaries, source data, extended data, supplementary information,

acknowledgements, peer review information; details of author contributions and competing interests; and statements of data and code availability are available at <https://doi.org/10.1038/s41586-020-2797-4>.

- Meilhac, S. M. & Buckingham, M. E. The deployment of cell lineages that form the mammalian heart. *Nat. Rev. Cardiol.* **15**, 705–724 (2018).
- Svensson, V., Vento-Tormo, R. & Teichmann, S. A. Exponential scaling of single-cell RNA-seq in the past decade. *Nat. Protoc.* **13**, 599–604 (2018).
- Wang, L. *et al.* Single-cell reconstruction of the adult human heart during heart failure and recovery reveals the cellular landscape underlying cardiac function. *Nat. Cell Biol.* **22**, 108–119 (2020).
- Tucker, N. R. *et al.* Transcriptional and Cellular Diversity of the Human Heart. *Circulation* (2020) <https://doi.org/10.1161/CIRCULATIONAHA.119.045401>.
- Chung Anne K. *et al.* Women Have Higher Left Ventricular Ejection Fractions Than Men Independent of Differences in Left Ventricular Volume. *Circulation* **113**, 1597–1604 (2006).
- Johnson, E. K., Matkovich, S. J. & Nerbonne, J. M. Regional Differences in mRNA and lncRNA Expression Profiles in Non-Failing Human Atria and Ventricles. *Sci. Rep.* **8**, 13919 (2018).
- Delplancq, G. *et al.* Cardiomyopathy due to PRDM16 mutation: First description of a fetal presentation, with possible modifier genes. *Am. J. Med. Genet. C Semin. Med. Genet.* (2020) <https://doi.org/10.1002/ajmg.c.31766>.
- Kim, S.-Y., Yasuda, S., Tanaka, H., Yamagata, K. & Kim, H. Non-clustered protocadherin. *Cell Adh. Migr.* **5**, 97–105 (2011).
- Donlin, L. T. *et al.* Smyd2 controls cytoplasmic lysine methylation of Hsp90 and myofibrillar organization. *Genes Dev.* **26**, 114–119 (2012).
- Mazzotta, S. *et al.* Distinctive Roles of Canonical and Noncanonical Wnt Signaling in Human Embryonic Cardiomyocyte Development. *Stem Cell Reports* **7**, 764–776 (2016).
- Shenton, F. C. & Pyner, S. Expression of transient receptor potential channels TRPC1 and TRPV4 in venoatrial endocardium of the rat heart. *Neuroscience* **267**, 195–204 (2014).
- Gao, M. *et al.* Conserved expression of the PRELI domain containing 2 gene (*Prelid2*) during mid-later-gestation mouse embryogenesis. *J. Mol. Biol.* **40**, 227–233 (2009).
- Putku, M. *et al.* CDH13 promoter SNPs with pleiotropic effect on cardiometabolic parameters represent methylation QTLs. *Hum. Genet.* **134**, 291–303 (2015).
- Liu, R. & Jin, J.-P. Calponin isoforms CNN1, CNN2 and CNN3: Regulators for actin cytoskeleton functions in smooth muscle and non-muscle cells. *Gene* **585**, 143–153 (2016).
- Besnard, S. *et al.* Smooth muscle dysfunction in resistance arteries of the staggerer mouse, a mutant of the nuclear receptor RORalpha. *Circ. Res.* **90**, 820–825 (2002).
- Mikhailov, A. T. & Torrado, M. The enigmatic role of the ankyrin repeat domain 1 gene in heart development and disease. *Int. J. Dev. Biol.* **52**, 811–821 (2008).
- Kwapiszewska, G. *et al.* Fhl-1, a new key protein in pulmonary hypertension. *Circulation* **118**, 1183–1194 (2008).
- Geng, T. *et al.* H19 lncRNA Promotes Skeletal Muscle Insulin Sensitivity in Part by Targeting AMPK. *Diabetes* **67**, 2183–2198 (2018).
- Huang, L. *et al.* Critical Roles of Xirp Proteins in Cardiac Conduction and Their Rare Variants Identified in Sudden Unexplained Nocturnal Death Syndrome and Brugada Syndrome in Chinese Han Population. *J. Am. Heart Assoc.* **7**, (2018).
- Fittipaldi, S. *et al.* Alpha B-crystallin induction in skeletal muscle cells under redox imbalance is mediated by a JNK-dependent regulatory mechanism. *Free Radic. Biol. Med.* **86**, 331–342 (2015).
- Rajakumari, S. *et al.* EBF2 determines and maintains brown adipocyte identity. *Cell Metab.* **17**, 562–574 (2013).
- 2016 AHA Late-Breaking Basic Science Abstracts. *Circ. Res.* **119**, e160–e171 (2016).
- Bolotta, A. *et al.* New Insights into the Hepcidin-Ferroportin Axis and Iron Homeostasis in iPSC-Derived Cardiomyocytes from Friedreich's Ataxia Patient. *Oxid. Med. Cell. Longev.* **2019**, 7623023 (2019).
- Lakhal-Littleton, S. *et al.* An essential cell-autonomous role for hepcidin in cardiac iron homeostasis. *Life* **5**, (2016).
- Medioni, C. *et al.* Expression of Slit and Robo genes in the developing mouse heart. *Dev. Dyn.* **239**, 3303–3311 (2010).
- Lee, J. H., Protze, S. I., Laksman, Z., Backx, P. H. & Keller, G. M. Human Pluripotent Stem Cell-Derived Atrial and Ventricular Cardiomyocytes Develop from Distinct Mesoderm Populations. *Cell Stem Cell* **21**, 179–194.e4 (2017).
- Liu, C., Luo, N., Tung, C.-Y., Perrin, B. J. & Zhao, B. GRXCR2 Regulates Taperin Localization Critical for Stereocilia Morphology and Hearing. *Cell Rep.* **25**, 1268–1280.e4 (2018).
- Liu, X. *et al.* Single-Cell RNA-Seq of the Developing Cardiac Outflow Tract Reveals Convergent Development of the Vascular Smooth Muscle Cells. *Cell Rep.* **28**, 1346–1361.e4 (2019).
- Kalucka, J. *et al.* Single-Cell Transcriptome Atlas of Murine Endothelial Cells. *Cell* **180**, 764–779.e20 (2020).
- Pober, J. S., Merola, J., Liu, R. & Manes, T. D. Antigen Presentation by Vascular Cells. *Front. Immunol.* **8**, 1907 (2017).
- Corada, M., Morini, M. F. & Dejana, E. Signaling pathways in the specification of arteries and veins. *Arterioscler. Thromb. Vasc. Biol.* **34**, 2372–2377 (2014).
- Kashiwazaki, M. *et al.* A high endothelial venule-expressing promiscuous chemokine receptor DARC can bind inflammatory, but not lymphoid, chemokines and is dispensable for lymphocyte homing under physiological conditions. *Int. Immunol.* **15**, 1219–1227 (2003).
- Awwad, K. *et al.* Role of secreted modular calcium-binding protein 1 (SMOC1) in transforming growth factor β signalling and angiogenesis. *Cardiovasc. Res.* **106**, 284–294 (2015).
- Tang, J. *et al.* Genetic Fate Mapping Defines the Vascular Potential of Endocardial Cells in the Adult Heart. *Circ. Res.* **122**, 984–993 (2018).
- Stallcup, W. B. The NG2 Proteoglycan in Pericyte Biology. *Adv. Exp. Med. Biol.* **1109**, 5–19 (2018).

36. Chen, Q. *et al.* Endothelial cells are progenitors of cardiac pericytes and vascular smooth muscle cells. *Nat. Commun.* **7**, 12422 (2016).
37. Barker, N. & Clevers, H. Leucine-rich repeat-containing G-protein-coupled receptors as markers of adult stem cells. *Gastroenterology* **138**, 1681–1696 (2010).
38. Daniel, J.-M. *et al.* Regulator of G-Protein Signaling 5 Prevents Smooth Muscle Cell Proliferation and Attenuates Neointima Formation. *Arterioscler. Thromb. Vasc. Biol.* **36**, 317–327 (2016).
39. Vanlandewijck, M. *et al.* A molecular atlas of cell types and zonation in the brain vasculature. *Nature* **554**, 475–480 (2018).
40. Sweeney, M. & Foldes, G. It Takes Two: Endothelial-Perivascular Cell Cross-Talk in Vascular Development and Disease. *Front Cardiovasc Med* **5**, 154 (2018).
41. Zhou, B. *et al.* Adult mouse epicardium modulates myocardial injury by secreting paracrine factors. *J. Clin. Invest.* **121**, 1894–1904 (2011).
42. Burstein Brett, Libby Eric, Calderone Angelino & Nattel Stanley. Differential Behaviors of Atrial Versus Ventricular Fibroblasts. *Circulation* **117**, 1630–1641 (2008).
43. Zhang, F., Li, C., Halfter, H. & Liu, J. Delineating an oncostatin M-activated STAT3 signaling pathway that coordinates the expression of genes involved in cell cycle regulation and extracellular matrix deposition of MCF-7 cells. *Oncogene* **22**, 894–905 (2003).
44. Lim, H. Y. *et al.* Hyaluronan Receptor LYVE-1-Expressing Macrophages Maintain Arterial Tone through Hyaluronan-Mediated Regulation of Smooth Muscle Cell Collagen. *Immunity* **49**, 326–341.e7 (2018).
45. Dick, S. A. *et al.* Self-renewing resident cardiac macrophages limit adverse remodeling following myocardial infarction. *Nat. Immunol.* **20**, 29–39 (2019).
46. Jaitin, D. A. *et al.* Lipid-Associated Macrophages Control Metabolic Homeostasis in a Trem2-Dependent Manner. *Cell* **178**, 686–698.e14 (2019).
47. Nahrendorf, M., Pittet, M. J. & Swirski, F. K. Monocytes: protagonists of infarct inflammation and repair after myocardial infarction. *Circulation* **121**, 2437–2445 (2010).
48. Heinrichs, D. *et al.* Macrophage migration inhibitory factor (MIF) exerts antifibrotic effects in experimental liver fibrosis via CD74. *Proc. Natl. Acad. Sci. U. S. A.* **108**, 17444–17449 (2011).
49. Valiño-Rivas, L. *et al.* CD74 in Kidney Disease. *Front. Immunol.* **6**, 483 (2015).
50. Hortells, L., Johansen, A. K. Z. & Yutzey, K. E. Cardiac Fibroblasts and the Extracellular Matrix in Regenerative and Nonregenerative Hearts. *J. Cardiovasc Dev Dis* **6**, (2019).
51. Bajpai, G. *et al.* The human heart contains distinct macrophage subsets with divergent origins and functions. *Nat. Med.* **24**, 1234–1245 (2018).
52. Kegel, L., Aunin, E., Meijer, D. & Bermingham, J. R. LGI proteins in the nervous system. *ASN Neuro* **5**, 167–181 (2013).
53. Struk, A. A. *et al.* Self-regulation and the foraging gene (PRKG1) in humans. *Proc. Natl. Acad. Sci. U. S. A.* **116**, 4434–4439 (2019).
54. Sahara, M. *et al.* Population and Single-Cell Analysis of Human Cardiogenesis Reveals Unique LGR5 Ventricular Progenitors in Embryonic Outflow Tract. *Dev. Cell* **48**, 475–490.e7 (2019).
55. Lerman, B. B. Outflow tract ventricular arrhythmias: An update. *Trends Cardiovasc. Med.* **25**, 550–558 (2015).
56. Dagda, R. K. *et al.* The spinocerebellar ataxia 12 gene product and protein phosphatase 2A regulatory subunit Bbeta2 antagonizes neuronal survival by promoting mitochondrial fission. *J. Biol. Chem.* **283**, 36241–36248 (2008).
57. Wang, L. *et al.* Polymorphisms of the tumor suppressor gene LSAMP are associated with left main coronary artery disease. *Ann. Hum. Genet.* **72**, 443–453 (2008).
58. Bruce, K. D. *et al.* Lipoprotein Lipase Is a Feature of Alternatively-Activated Microglia and May Facilitate Lipid Uptake in the CNS During Demyelination. *Front. Mol. Neurosci.* **11**, 57 (2018).
59. Kim, H.-S. *et al.* Schwann Cell Precursors from Human Pluripotent Stem Cells as a Potential Therapeutic Target for Myelin Repair. *Stem Cell Reports* **8**, 1714–1726 (2017).
60. Antonopoulos, A. S. & Antoniadis, C. The role of epicardial adipose tissue in cardiac biology: classic concepts and emerging roles. *J. Physiol.* **595**, 3907–3917 (2017).
61. Vijay, J. *et al.* Single-cell analysis of human adipose tissue identifies depot and disease specific cell types. *Nat Metab* **2**, 97–109 (2020).
62. Hepler, C. *et al.* Identification of functionally distinct fibro-inflammatory and adipogenic stromal subpopulations in visceral adipose tissue of adult mice. *Elife* **7**, (2018).
63. Hoffmann, M. *et al.* SARS-CoV-2 Cell Entry Depends on ACE2 and TMPRSS2 and Is Blocked by a Clinically Proven Protease Inhibitor. *Cell* (2020) <https://doi.org/10.1016/j.cell.2020.02.052>.
64. Watanabe, K., Umičević Mirkov, M., de Leeuw, C. A., van den Heuvel, M. P. & Posthuma, D. Genetic mapping of cell type specificity for complex traits. *Nat. Commun.* **10**, 3222 (2019).
65. Leid, J. *et al.* Primitive Embryonic Macrophages are Required for Coronary Development and Maturation. *Circ. Res.* **118**, 1498–1511 (2016).
66. Chen, B., Brickshawana, A. & Frangogiannis, N. G. The Functional Heterogeneity of Resident Cardiac Macrophages in Myocardial Injury CCR2+ Cells Promote Inflammation, Whereas CCR2- Cells Protect. *Circulation research* vol. **124** 183–185 (2019).
67. Vaduganathan, M. *et al.* Renin-Angiotensin-Aldosterone System Inhibitors in Patients with Covid-19. *N. Engl. J. Med.* **382**, 1653–1659 (2020).

Publisher's note Springer Nature remains neutral with regard to jurisdictional claims in published maps and institutional affiliations.



Open Access This article is licensed under a Creative Commons Attribution 4.0 International License, which permits use, sharing, adaptation, distribution and reproduction in any medium or format, as long as you give appropriate credit to the original author(s) and the source, provide a link to the Creative Commons license, and indicate if changes were made. The images or other third party material in this article are included in the article's Creative Commons license, unless indicated otherwise in a credit line to the material. If material is not included in the article's Creative Commons license and your intended use is not permitted by statutory regulation or exceeds the permitted use, you will need to obtain permission directly from the copyright holder. To view a copy of this license, visit <http://creativecommons.org/licenses/by/4.0/>.

© The Author(s) 2020

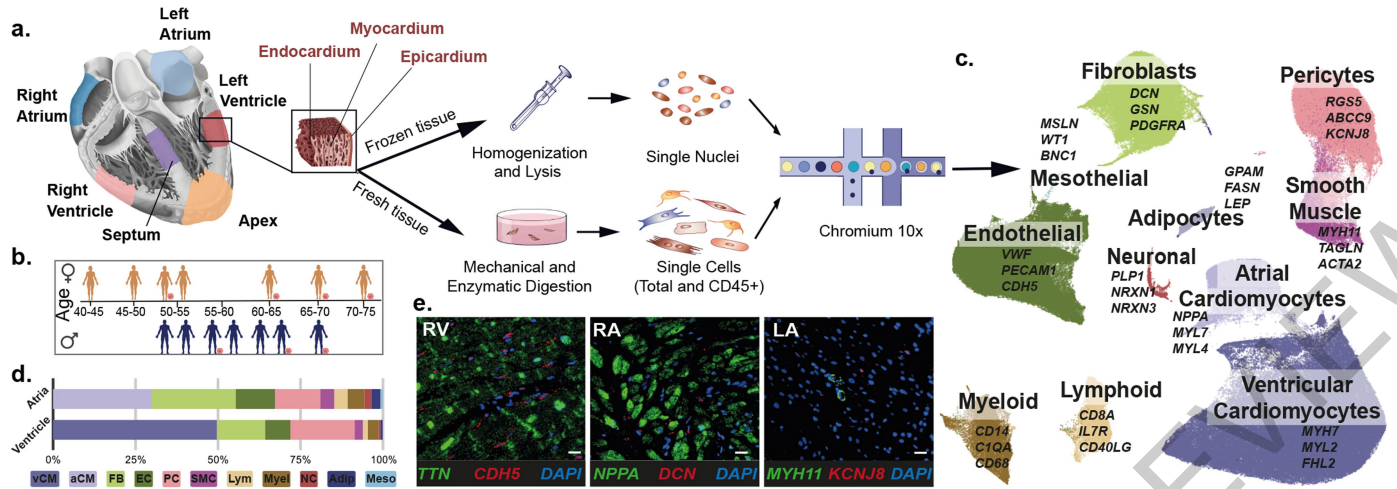


Fig. 1 | Cell composition of the adult human heart. **a.** Transmurals were obtained from RA, LA, RV, LV, AX and SP from 14 individuals. Single nuclei (n = 14) and single cells (n = 7) were processed using Chromium 10X 3' DEG chemistry. **b.** Infographic shows donors (women, top; men, bottom), age, and contribution to cells and nuclei datasets (orange circle) (Data available in Supplementary Table 1) **c.** UMAP embedding of 487,106 cells and nuclei delineate 11 cardiac cell types and marker genes. **d.** Distribution of cell

populations, identified from nuclei within atria (LA, RA) and ventricles (LV, AX, SP, RV) after subclustering analysis. Color code corresponds to **c** (Data available in Supplementary Table 2). **e.** Multiplexed smFISH of cell type-specific transcripts in RV (left): *TTN* (green, CM) and *CDH5* (red, EC) RA (middle): *NPPA* (green, aCM) and *DCN* (red, FB) and LA (right): *MYH11* (green, SMC) and *KCNJ8* (red, PC), nuclei are DAPI-stained (dark blue). Scale bar 20 μm. For details on statistics and reproducibility, please see **Methods**.

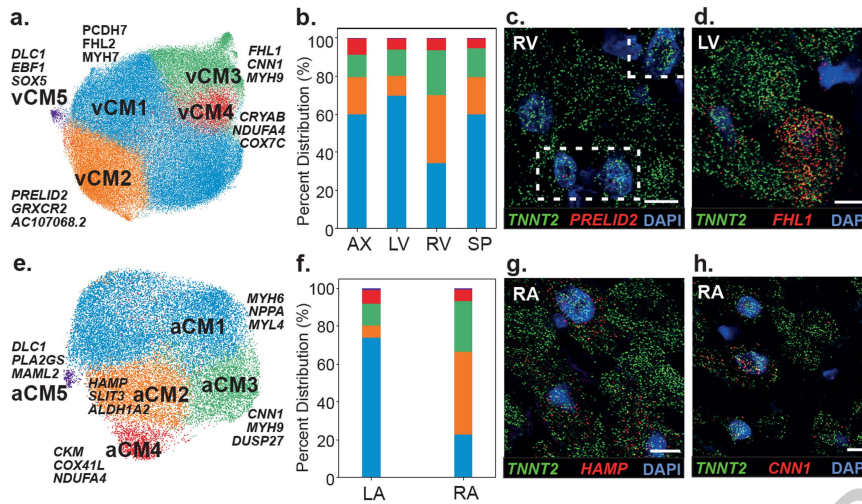


Fig. 2 | Cardiomyocytes. a. UMAP embedding of five vCM populations **b.** Regional distributions of vCM populations (Data available in Supplementary Table 5). **c.** Multiplexed smFISH of *PRELID2* (red) enriched in vCM2 and **d.** of *FHL1* (red) enriched in vCM3. **g.** Multiplexed smFISH of *HAMP* (red) enriched in

aCM2 and **h.** of *CNN1* (red) enriched in aCM3. **c., d.** and **g., h.** *TNNT2* expression in green, nuclei are DAPI-stained (dark blue). Scale bar 10 μ m. For details on statistics and reproducibility, please see **Methods**.

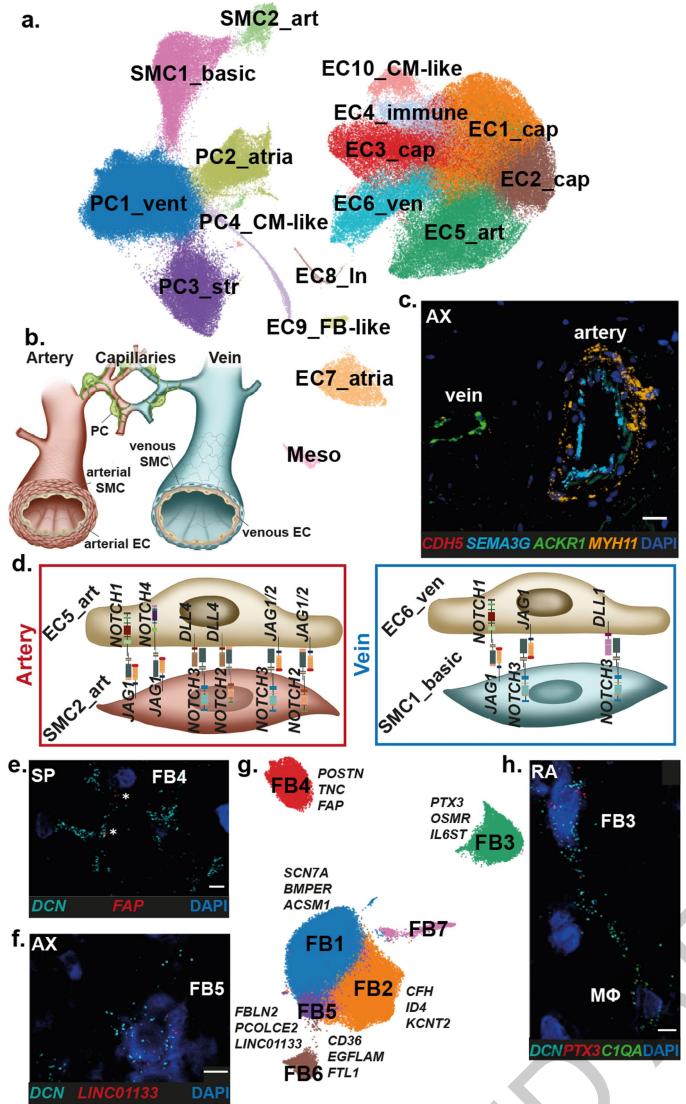


Fig. 3 | Vascular, stromal and mesothelial cells. **a.** UMAP embedding of 17 vascular and mesothelial populations. EC1/2/3_cap, capillary EC; EC4_immune, immune-related EC; EC5_art, arterial EC; EC6_ven, venous EC; EC7_atria, atria-enriched EC; EC8_In, lymphatic EC; EC9_FB-like, EC with FB features; EC10_CM-like, EC with CM features; PC1_vent, ventricle-enriched PC; PC2_atria, atria-enriched PC; PC3_str, stromal PC; PC4_CM-like, PC with CM features; SMC1_basic, basic SMC; SMC2_art, arterial SMC; Meso, mesothelial cells. **b.** Schematic of the vascular cells and their placement in the vasculature. **c.** Multiplexed smFISH of *MYH11* (yellow) in SMC (thick in artery and very thin in small vein), *CDH5* (red) in the endothelium, and *SEMA3G* (cyan) and *ACKR1* (green) in EC5_art and EC6_ven respectively in AX, nuclei are DAPI-stained (dark blue). Scale bar 20 μ m. **d.** Predicted cell-cell interactions in arteries and veins (Data available in Supplementary Table 10). **e., f.** Multiplexed smFISH of pan-FB *DCN* (cyan) and *e. FAP* (red) in FB4 in SP and *f. LINC001133* (red) in FB5 in AX. Nuclei are DAPI-stained (dark blue). Scale bar 5 μ m. **g.** UMAP embedding showing six FB populations and their respective marker genes. **h.** Multiplexed smFISH of *C1QA*+ macrophages (M Φ) and *PTX3*+ FB3 suggesting cross-talk between both cell types, nuclei are DAPI-stained (dark blue). Scale bar 5 μ m. For details on statistics and reproducibility, please see **Methods**.

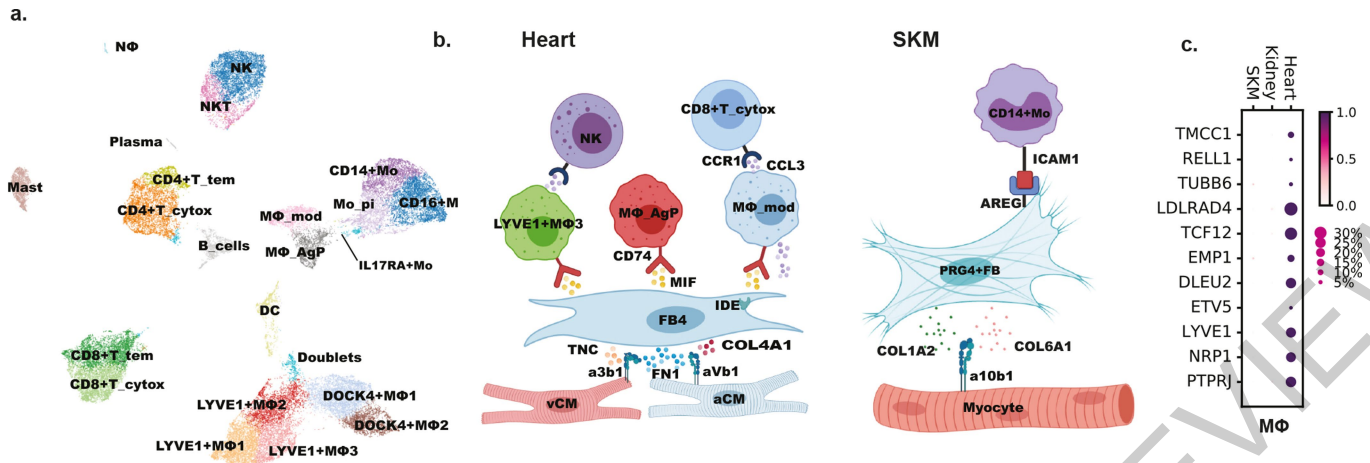


Fig. 4 | Cardiac immune populations and cell-cell interactions. **a.** Manifold of 40,868 myeloid and lymphoid cardiac cells. NΦ, neutrophils; NK, Natural killer; NKT, Natural killer T cells; CD4+T_naive, Naive CD4+ T cells; CD4+T_cyt, CD4+ cytotoxic T cells; CD8+T_tem, CD8+ effector-memory T cells; CD8+T_cyt, CD8+ cytotoxic T cells; DC: Dendritic cells; CD14+Mo, CD14+ monocytes; CD16+Mo, CD16+ monocytes; Mo_pi, pro-inflammatory monocytes; IL17RA+Mo, IL17RA+ monocytes; MΦ_AgP, HLA class II antigen-presenting MΦ; MΦ_mod, monocyte-derived MΦ; LYVE1+MΦ1-3,

M2-like, LYVE1+ MΦ set 1-3; *DOCK4*+MΦ1-2, *DOCK4*+MΦ set 1-2; doublets: doublets; B_cells, B cells; Plasma, plasma B cells. **b.** BioRender® infographic summarizes predicted cell-cell interaction circuits between aCM and vCM, FB4, and immune cells involved in tissue repair in the heart and skeletal muscle (SKM) (Data available in Supplementary Table 17). **c.** Gene expression signature for cardiac-specific LYVE1+MΦ compared against predicted matched populations in SKM and Kidney.

Article

Methods

Experimental methods

Research ethics for donor tissues. Heart tissues (D1-7 and 11) are processed at Wellcome Sanger Institute (Hinxton, UK) are obtained from deceased transplant organ donors after Research Ethics Committee approval (Ref 15/EE/0152, East of England - Cambridge South Research Ethics Committee) and informed consent from the donor families. Heart tissues (H2-7) are processed at Harvard Medical School (Boston, MA, USA) are obtained from deceased organ donors after Human Research Ethics Board approval Pro00011739 (University of Alberta, Edmonton, Canada). Informed consent from donor families is acquired *via* the institutional Human Organ Procurement and Exchange Program (HOPE). Cardiovascular history was unremarkable for all donors (Supplementary Table 1).

Tissue acquisition and processing. Tissue is acquired from UK and North American donors (D1-7 and 11, H2-7) after circulatory death (DCD: D2, D4-7 and D11) and after brain death (DBD: D1, D3, H2-7). For UK DCD donors after a five minute stand-off and for DBD, the chest is opened, the aorta is cross-clamped and cardiac samples are acquired. For North American DBD donors, the aorta is cross-clamped, cold cardioplegia (Celsior) is administered under pressure via the aorta to arrest beating, the heart is excised, rinsed in cold saline and samples acquired. All donor samples are full-thickness myocardial biopsies from LA, RA, RV, SP, AX and LVs, with intentional exclusion of large epicardial fat deposits. Samples used for single nuclei isolation are flash-frozen and stored at -80 °C. Single cell isolation and CD45+ enrichment is carried out on freshly collected samples. Residual tissue after nuclei and cell isolation procedures is formalin-fixed or frozen in OCT for additional studies.

All our tissues were stored and transported on ice at all times until freezing or tissue dissociation to minimise any transcriptional degradation. Previous studies on the post-mortem tissue stability of the GTEx consortium on bulk tissues⁶⁸ and in single cells⁶⁹ suggest only minor changes in tissues within the first 24h post-mortem when stored in cold conditions.

Single nuclei isolation. Single nuclei are obtained from flash-frozen tissues using mechanical homogenization as previously described⁷⁰. Tissues are homogenized using a 7 ml glass Dounce tissue grinder set (Merck) with 8-10 strokes of a loose pestle (A) and 8-10 strokes of a tight pestle (B) in homogenization buffer (250 mM Sucrose, 25 mM KCl, 5 mM MgCl₂, 10 mM Tris-HCl, 1 mM dithiothreitol (DTT), 1x Protease Inhibitor, 0.4 U/μl RNaseIn, 0.2 U/μl SUPERaseIn, 0.1% Triton X-100 in nuclease-free water). Homogenate is filtered through a 40 μm cell strainer (Corning). After centrifugation (500×g, 5 min, 4 °C) the supernatant is removed and the pellet is resuspended in storage buffer (1x phosphate-buffered saline (PBS), 4% bovine serum albumin (BSA), 0.2 U/μl Protector RNaseIn). Nuclei are stained with NucBlue Live ReadyProbes Reagents (ThermoFisher) and Hoechst-positive single nuclei are purified by fluorescent activated cell sorting using Influx, XDP or FACSAria (BD Biosciences) (Supplementary Figure 1). Nuclei purification and integrity is verified under microscope and they are further processed using the Chromium Controller (10X Genomics) according to the manufacturer's protocol.

Single cell preparation. Heart tissues (0.2-0.9 g) are transferred from cardioplegic solution into gentleMACS C-tubes (Miltenyi Biotec) containing enzymatic digestion base solution (100 μgml⁻¹ Liberase TH Research grade and 50 μgml⁻¹ DNase I, HBSS 10 mM HEPES, 30 mM taurine)⁷¹. Tissues are minced using scissors (FST) and automatically digested using gentleMACS Octo Dissociator (Miltenyi Biotec) with heaters. Cardiomyocyte-depleted single-cell suspension are washed with base solution containing 20% fetal bovine serum (FBS, Gibco),

filtered through 70 μm nylon strainer (BD Falcon), collected by centrifugation (330×g, 10 min, 4 °C) and resuspended in base solution containing 0.2% FBS (Gibco). Cells are manually counted three times by Trypan blue exclusion after each centrifugation and resuspended at a concentration of $\geq 2 \times 10^6$ /ml. Single cells are processed using Chromium Controller (10X Genomics) according to the manufacturer's protocol.

CD45+ cell enrichment. Cell suspension is prepared as described above and subsequently are labelled using anti-human CD45 monoclonal antibody-conjugated microbeads according to the manufacturer's protocol (Miltenyi Biotec). Briefly, up to 10^7 cells are incubated for 15 min at 4 °C in 80 μl of PBS/BSA/EDTA buffer (1x PBS pH 7.2, 0.5% BSA, 2 mM EDTA) containing 20 μl CD45 microbeads. Cell suspension is washed in PBS/BSA/EDTA buffer once and harvested by centrifugation (330×g, 10 min, 4 °C). Resuspended cells are applied to MACS LS columns (Miltenyi Biotec). CD45-depleted cell fraction is discarded after three washes with PBS/BSA/EDTA buffer and CD45+ cell fraction is collected in PBS/BSA/EDTA buffer by removal of the columns from the magnetic field. CD45+ cells are counted and resuspended in PBS/BSA/EDTA buffer to a concentration of $\geq 2 \times 10^6$ /ml before further processing using a Chromium Controller (10X Genomics) according to the manufacturer's protocol.

Chromium 10X library preparation. Single cells and nuclei are manually counted by Trypan blue exclusion or automatically using a Countess II (Life Technologies) using at least two separate counts. Cell or nuclei suspension is adjusted to 400-1,000 cells/μl and loaded on the Chromium Controller (10X Genomics) with a targeted cell/nuclei recovery of 4,000-10,000 per reaction. 3' gene expression libraries are prepared according to the manufacturer's instructions of the v2 or v3 Chromium Single Cell Reagent Kits (10X Genomics). Quality control of cDNA and final libraries is done using Bioanalyzer High Sensitivity DNA Analysis (Agilent) or 4200 TapeStation System (Agilent). Libraries are sequenced using HiSeq 4000 (Illumina) at Wellcome Sanger Institute, and NextSeq 500 (Illumina) at Harvard Medical School with a minimum depth of 20,000-30,000 read pairs per cell or nucleus (Supplementary Table 22).

Spatial validation using smFISH with RNAscope probes. During preparation of formalin-fixed paraffin-embedded (FFPE) samples fresh tissue is fixed in neutral-buffered 10% formalin for 18-36 hrs and subsequently embedded in paraffin blocks. Fixed-frozen (FF) tissue samples are fixed in 4% paraformaldehyde (ThermoFisher). Sections are cut at 5 μm thickness using a microtome, and are placed onto SuperFrost Plus slides (VWR). FFPE tissue slides are automatically stained using BOND RX (Leica) and the RNAscope Multiplex Fluorescent Reagent Kit v2 Assay (ACDBio) according to the manufacturer's protocol. FF tissue slides are processed according to the protocol of RNAscope Multiplex Fluorescent Assay v1 (ACDBio). RNAscope ready- or custom-made target probes are run in parallel to multiplex positive and negative controls (Extended Data Figure 12b, Supplementary Table 23). All nuclei are DAPI-stained. All FFPE tissue slides are imaged using an Opera Phenix High-Content confocal Screening System (Perkin Elmer) with 1 μm z-step size and 20× water-immersion objective (NA 0.16, 0.299 μm/pixel). Channels: DAPI (Excitation 375 nm, Emission 435-480 nm), Atto 425 (Excitation 425 nm, Emission 463-501 nm), Opal 520 (Excitation 488 nm, Emission 500-550 nm), Opal 570 (Excitation 561 nm, Emission 70-630 nm), Opal 650 (Excitation 640 nm, Emission 650-760 nm). FF tissue slides are imaged using a LSM710 confocal microscope (Zeiss) and 40× oil-immersion objective (1.3 Oil, DIC III). Channels: DAPI (Excitation 375 nm, Emission 435-480 nm), Alexa Fluor 488 (Excitation 492 nm, Emission 517 nm), Atto 550 (Excitation 560 nm, Emission 575 nm) and Atto 647 (Excitation 649 nm, Emission 662 nm). Visualization and background removal (rolling ball radius) are done using Fiji/ImageJ⁷². Pseudocolors were used for better visualization.

Hematoxylin and eosin staining. Tissue samples are fresh-frozen in isopentane (ThermoFisher) at -80 °C and OCT (VWR) embedded. Sections are cut at a thickness of 10 µm using a microtome, placed onto SuperFrostPlus slides (VWR) and further processed according to standard hematoxylin and eosin staining protocol (Extended Data Figure 12a).

Skeletal muscle tissue acquisition. Intercostal muscle samples are obtained from between the 2nd and 3rd rib on the left side. This is typically from the deepest layer of muscle (furthest away from the skin). Samples are collected directly into the cold preservation solution.

Nuclei isolation for skeletal muscle. Muscle tissue is washed in 1x PBS, is cleaned of any visible fat depositions and is minced to obtain fragments of approximately 1 mm³. Per each sample, ~0.3 g of minced tissues is homogenised in 3 ml of Buffer A (250 mM sucrose, 10 mg/ml BSA, 5 mM MgCl₂, 0.12 U/µl RNaseIn, 0.06 U/µl SUPERasin, 1x Protease Inhibitor) using Dounce tissue grinder set (Merck) with 50 strokes of the loose pestle (A). The homogenate is filtered through a 100 µm cell strainer (Corning) and the strainer is washed twice with 1 ml and with 750 µl of Buffer A. After adding Triton X-100 (final concentration 0.5%), the mixture is further homogenised with 50 strokes of the tight pestle (B). Following filtering through a 40 µm strainer, nuclei are centrifuged (3000×g, 5 min, 4 °C), resuspended in 1 ml of Buffer B (320 mM Sucrose, 10 mg/ml BSA, 3 mM CaCl₂, 2 mM MgAc₂, 0.1 mM EDTA, 10 mM Tris-HCl, 1 mM DTT, 1x Protease Inhibitor, 0.12 U/µl RNaseIn, 0.06 U/µl SUPERasin) and purified using a 27% percoll gradient solution. The percoll mixture is centrifuged at (20,000×g, 15 min, 4°C) and the pellet is resuspended in 200 µL of Buffer B, followed by centrifugation (20,000×g, 3 min, 4°C). After Trypan Blue staining, the intact nuclei are counted using a hemocytometer. Nuclei are profiled using a Chromium Controller (10X Genomics) according to the manufacturer's protocol.

Single cell isolation for skeletal muscle. Muscle tissue is washed in 1x PBS, cleaned of any visible fat depositions and finely minced. 2 g of the minced tissue is transferred to digestion buffer 1 (750 U/ml Collagenase type 2 in 1x PBS) and incubated at 37°C in a water bath for 90 min. The partially digested tissue is collected by centrifugation (650×g, 5 min, 4°C) and the pellet is resuspended in digestion buffer 2 (100 U/ml Collagenase type 2, 2 U/ml Dispase in PBS). After 30 min incubation at 37°C in a water bath, the digestion is stopped by adding 2% FBS. Cells are filtered through a 100 µm and a 40 µm nylon strainer (BD Falcon), collected by centrifugation (650×g, 4°C, 3 min) and washed with 1x PBS/ 2% FBS. Subsequently, 20% percoll gradient (15,000×g, 4°C, 20 min) is used for cells' purification. The layer containing cells is collected, washed in PBS containing 2% FBS and viable cells are counted by Trypan Blue exclusion using a hemocytometer. Nuclei are profiled using a Chromium Controller (10X Genomics) according to the manufacturer's protocol.

The methods key resources table is found in Supplementary Table 24.

Data analysis

Transcriptome mapping. After sequencing, samples are demultiplexed and stored as CRAM files. Each sample is mapped to the human reference genome (GRCh38 v3.0.0) provided by 10X Genomics, and using the Cell Ranger suite (v3.0.1) with default parameters. Single cell samples are mapped against the reference as it was provided. Single nuclei samples, the reference for *pre-mRNA* is created using the 10X Genomics instructions (<https://support.10xgenomics.com/single-cell-gene-expression/software/pipelines/latest/advanced/references>).

Count data processing. After mapping, samples from each data source (single nuclei, single cell and CD45+ cell) are grouped into individual

AnnData objects by concatenating the raw_feature_bc_matrix_h5.h5 and adding the appropriate metadata information. For each data source object, the mean of UMIs (n_counts) is calculated and used as a threshold for empty droplets.

Doublet detection. After empty droplets removal, we applied scrublet⁷³ to assign a doublet score (scrublet_score) to each cell. These cells are clustered and visualised using the UMAP method⁷⁴. Additionally, each cell is processed for doublet detection using a percolation method to allow for improved detection of doublets⁷⁵.

Cell QC and filtering. Each data source is processed and annotated separately to account for source-specific quality differences. These metrics are included as covariates for further processing. Total cells and CD45+ cells are filtered for counts (500 < n_counts < 15000), genes (200 < n_genes), mitochondrial genes (percent_mito < 20%), ribosomal genes (percent_ribo < 20%) and scrublet score (scrublet_score < 0.3). Single nuclei are filtered for counts (500 < n_counts < 15000), genes (300 < n_genes < 6000), mitochondrial genes (percent_mito < 5%), ribosomal genes (percent_ribo < 5%) and scrublet score (scrublet_score < 0.3). The same filtering thresholds are applied to the skeletal muscle dataset.

Scanpy toolkit 1.5⁷⁶ in Python version 3.7 is used to perform downstream analyses, including normalization (normalize_per_cell: counts_per_cell_after = 10,000), log transformation (log1p), variable gene detection (highly_variable_genes), regressing out unwanted sources of variation (regress_out: n_counts and percent_mito), data feature scaling (scale: max_value = 10) and PCA (pca: using highly variable genes) as previously described⁷⁷.

Batch alignment using deep variational autoencoder. We build a global manifold by aligning all the data sources and donors in our data. This is done in a three-step procedure: **a)** Each source is analysed and annotated separately aligning only for donors using a PC-space linear regression step prior to batch alignment with *bbknn*⁷⁸. DEGs are calculated using a Wilcoxon Rank Sum Test with Bonferroni-Hochberg adjustment as implemented in the *Scanpy* framework. **b)** To annotate each cluster, we use an integrative approach by searching the top significant DEGs (*p*-value < 1e-05) with a logFC > 1 against the *ToppFun*⁷⁹ and *EnrichR*⁸⁰ databases. Significant hits on *Pathways*, *Transcriptional regulation* and *Biological processes* are prioritised to annotate a given cluster. Each cellular compartment is labelled under the adata.obs['cell_type'] slot after grouping source-specific cell states. **c)** All sources are combined into a single AnnData object under the label adata.obs['cell_sources']. Batches are aligned using the *batch_correction* function from the *scGen* variational autoencoder⁸¹. First we align for adata.obs['cell_sources'], using adata.obs['cell_type'] as an anchor. Next we align for adata.obs['donor'], using adata.obs['cell_type'] as an anchor. Each batch alignment round is run for 50 epochs.

Manifolds for the adipocytes, vascular and immune cardiac populations, as well as the skeletal muscle analysis are created using this method and the clustering accuracy is evaluated with SCCAF⁸² (Extended Data Figure 12d).

Detection of differentially expressed genes (DEGs). To help with the annotation of the subpopulations of each cell compartment, we calculate the DEGs using the Wilcoxon Rank Sum test as implemented in the *scanpy* workflow and recommended by recent benchmarking studies⁸³. A gene is considered to be differentially expressed if it has a log₂FC > 1 and a *p*-value < 1e-05, unless stated otherwise in the analysis section.

Cell-Cell interactions. Expression matrices of the populations under study are exported from the AnnData, together with a metadata table that contain the cell-barcode as indices. We then run CellPhoneDB as

Article

follows: cellphonedb method statistical_analysis meta.tsv counts.tsv --counts-data=gene_name--threads=60. CellPhoneDB raw predictions are filtered by removing those interactions with a p -value $> 1.0e-05$. Significant pairs are then submitted for gene set enrichment analysis into ReactomeDB, enrichR and ToppFun for functional classification. The vascular cells are randomly sub-sampled to 39 000 cells before the analysis, and the cardiac repair group (aCM, vCM, FB and immune cells) is randomly sub-sampled to 69 295 cells before the analysis.

Visualisation of gene expression on 10X Genomics Visium data. We process the publicly available LV myocardium Visium data from 10X Genomics (https://support.10xgenomics.com/spatial-gene-expression/datasets/1.0.0/V1_Human_Heart) using the Scanpy v1.5 workflow adapted for the analysis of 10X Genomics Visium data (<https://scanpy-tutorials.readthedocs.io/en/latest/spatial/basic-analysis.html>). In brief, spots are removed with less than 500 UMIs or more than 20000 UMIs, and less than 200 genes. Data is log-transformed and normalised prior to plotting.

Estimation of RNA Velocity. To calculate the RNA velocity of the single cells and CD45+ enriched single cells, we use the CellRanger output BAM file and the GENCODE v33 GTF (ftp://ftp.ebi.ac.uk/pub/databases/genencode/Gencode_human/release_33/gencode.v33.chr_patch_hapl_scaff.annotation.gtf.gz) file together with the *velocity*⁸⁴ CLI v0.17.17 to generate a loom file containing the quantification of spliced and unspliced RNA. Next, we build a manifold, cluster the cells and visualise the RNA velocities using *scVelo*⁸⁵.

Subpopulation analyses of aCM, vCM, FB and NC. All barcodes labelled in the global object as cardiomyocytes, fibroblasts and neural cells are selected for further subpopulation analyses. Additional cell population-specific filtering criteria are applied to nuclei as follows: CM - counts ($n_counts < 12500$), genes ($n_genes < 4000$), mitochondrial genes ($percent_mito < 1\%$), ribosomal genes ($percent_ribo < 1\%$) and scrublet score ($scrublet_score < 0.25$); FB - mitochondrial genes ($percent_mito < 1\%$), ribosomal genes ($percent_ribo < 1\%$); NC - genes ($n_genes < 4000$), mitochondrial genes ($percent_mito < 1\%$), ribosomal genes ($percent_ribo < 1\%$). Total and CD45+ cells are excluded in the aCM and vCM datasets and do not contribute to subpopulation analysis. No further filtering of FB or NC total and CD45+ cells are applied. CM and FB are then further split into two groupings based on the region of origin: i) LA and RA and ii) LV, RV, AX and SP.

Donor effects are aligned as described in step a) above. For FB and NC, sources are aligned as described in step c) above. Leiden clustering and UMAP visualization are performed for identifying subpopulations and visualization⁸⁶. Differentially expressed genes are calculated using the Wilcoxon Rank-Sum test. Genes are ranked by score.

Cross-tissue comparison of cardiac immune populations with skeletal muscle, kidney and blood immune populations. We collect single cell transcriptome data for adult kidneys from Stewart *B et al* (2019) available here: <https://www.kidneycellatlas.org/>, and subset all immune cells reported in their study. For the SKM we select the annotated immune cells from the merged manifold. For the human blood, we used the publicly available 10K single PBMC cells dataset provided by 10X Genomics (https://support.10xgenomics.com/single-cell-gene-expression/datasets/3.0.0/pbmc_10k_v3). As previously described⁸⁷, we train a logistic regression model on the cardiac immune cells using 80% of the expression data and test its accuracy on the remaining 20% to produce a model with an accuracy of 0.6862 (Extended Data Figure 8f and Supplementary Table 16). We then apply this model to predict analogue cardiac immune populations in the adult kidney, SKM and PBMC. Predictions with a probability greater than 0.8 are excluded from downstream comparative analyses.

Gene Ontology enrichment analysis. For the vCM population we use the R package gProfileR (<https://cran.r-project.org/web/packages/gProfileR/index.html>) with the score-ranked gene list of vCM4 as input and the set of genes expressed in vCM as background (those genes having a UMI count > 1). To perform the gene ontology analysis on the vascular cells, the top 500 significant DEGs (p -value $< 1e-05$) with a $\log_{2}FC > 1$ are searched against the gene ontology biological process database using *ToppFun*⁷⁹ (Supplementary Table 25) The top 5 significantly enriched terms (q -value < 0.05) for each subpopulation are selected and plotted on a heatmap. To perform the pathway analysis on the adipocytes, the top 500 significant DEGs (p -value $< 1e-05$) with a $\log_{2}FC > 0.5$ are searched against *ToppFun*⁷⁹ pathway databases (Supplementary Table 26). The top 5 significantly enriched pathways (q -value < 0.05) for each subpopulation are selected and plotted on a heatmap.

Gene set score. We use the `score_genes` function as implemented in *scanpy* to calculate the enrichment of genes involved in the Oncostatin M pathway. A list of genes is collected upon literature research^{88,89}. For gene set enrichment, only highly expressed genes are considered to reduce noise (more than 500 UMIs across all cells). The same analysis is performed for comparison of cardiac immune cells in our study with the observations of previous studies on cardiac-resident M ϕ ⁵¹, murine tissue-remodeling M ϕ ⁴⁵ and yolk sac lineage origin⁹⁰.

Statistics and Reproducibility. All analyses are performed using *R Software, Version 3.6.1*. Student t-tests (t-tests) are used to compare cell type distributions at each site. A p -value < 0.05 is considered statistically significant. Linear regression models (correlations) are obtained using the R linear model function (`lm`), which estimates statistical likelihood (p -value) of a linear relationship. Bonferroni correction is applied for multiple testing.

The depicted RNAscope micrographs in the figures are representative. The micrographs in Figure 2g, 3c/h and Extended Data Figure 3c (**HAMP**), 3e (**CNN1**), 4g, 4m, 6f are repeated with similar results in 2 individual tissue sections. The micrographs in Figure 2h, 3f and Extended Data Figure 3c (**CNN1**), 3e (**PCDH7**), 6e, 6h, 9d are repeated with similar results in 3 individual tissue sections. The micrographs in Figure 1e, 2d, 3e, and Extended Data Figure 1f, 3c (**FHL1**) and 6d are repeated with similar results in 4 individual tissue sections. The micrographs in Figure 2c and Extended Data Figure 3c (**PRELID2**), 10e, 12a are repeated with similar results in 6 or more individual tissue sections. Positive and negative controls were done once per used samples.

GWAS enrichment analysis. We download GWAS summary statistics from broad cudi, EBI GWAS catalog and GWAS atlas. We select traits with well powered GWAS ($N > 5000$ and number of significant loci > 10). GWAS data sets are summarized in (Supplementary Table 27). Gene expression data of protein coding genes are mapped onto Entrez gene ids and these gene annotations are used on the human genome assembly hg19 / 37. We only use gene expression data from nuclei. We implement the analysis described in⁶⁴ in python and in R. The log transformed counts (plus one pseudocount) are used to compute average cell type specific expression profiles. We perform individual magma analyses for each cell type, always conditioning on default gene level covariates (e.g. gene length) and average gene expression across all cells. Subsequently we apply the Benjamini Hochberg method and select cell type trait associations with FDR $< 10\%$. These pairs are then subjected to conditional analysis as described in⁶⁴ to define “independent”, “jointly explained” and “partially jointly explained” pairs of associations (Supplementary Table 28).

Additional Analysis

Distributions of dispersed cells and isolated nuclei. The different procedures for obtaining isolated nuclei and dispersed cells result

in significantly different distributions of cell types (Supplementary Table 29 and Extended Data Figure 2). Notably, 30.1% and 49.2% of isolated nuclei are derived from aCM and vCM in the atrial and ventricular, while these cells were mostly excluded from preparations of isolated and CD45 selected cells (Supplementary Table 2).

Excluding CM, the distribution of cell types identified from isolated nuclei and dispersed cells remain distinct (Supplementary Table 30). While 59.0% of dispersed cells are EC, only 15.7% of nuclei are derived from EC. By contrast, 64.2% of nuclei are from FB (31.2%) and PC (33.0%) while only 17.1% of dispersed cells are FB (2.3%) and PC (14.8%). These differences may reflect sensitivity of EC nuclei to isolation procedures or resistance of PC and FB to cellular enzymatic digestion.

Despite differences in cell distributions between isolated nuclei and dispersed cells the gene expression profiles of cell lineages are reasonably correlated ($r > 0.4$ for each cell type). To address the concordance of the genes captured by cells and nuclei, we compared the expression of the major cell type markers from Figure 1c across the three sources (Extended Data Figure 1c). As nuclei lack cytoplasmic RNA, the expression of certain genes, especially immune genes *NK7G* and *CIQA*, was lower in nuclei compared to the cells. Nevertheless, the general trend with respect to marker genes was consistent across the three sources, and the same genes distinguished individual cell types independent of the source.

Further analysis of vascular cells. The PC3_str contains similar contribution of cells and nuclei, that has a scrublet score below the stringent threshold used, nevertheless the average number of genes and counts in the cell fractions is higher than average, thus, despite our stringent quality filtering, we cannot exclude there might be doublets in this cluster. EC10_CMC-like and PC4_CMC-like co-express EC or PC genes with CM markers and further studies are required to understand whether they represent previously unknown cell states or doublets.

The observations of the arterial and venous SMC is supported by previous studies, predicting arterial SMC as more contractile, and venous SMC as less differentiated.⁹¹

EC3_cap enrich for transcripts encoding components of AP1 (*JUN* and *FOS*), which mediates multiple EC fate decisions including response to VEGF, inflammatory and stress signals, and *ATF3*, an adaptive-response gene induced by diverse signals⁹²⁻⁹⁴.

Skeletal muscle characterisation. We collect intercostal skeletal muscle samples from five healthy individuals, including one donor with matched cardiac tissue, and profile the transcriptome of 35,665 single cells and 39,597 single nuclei. Analogously to the heart, the combination of cells and nuclei allow us to capture and resolve major cell lineages, including myocyte, fibroblasts, endothelial cells, smooth muscle cells, pericytes, myeloid and lymphoid immune cells and satellite cells (Extended Data Figure 11a,b and Supplementary Table 31).

Further analysis of the vascular cells of the skeletal muscle unveils 10 distinct populations. The endothelial cells show 5 clusters separated based on their respective vascular beds with signatures similar to the ones we observe in the heart. The EC_cap expresses VWF and RGCC. venous EC_ven express ACKR1 and PLVAP, while arterial EC_art show SEMA3G and HEY1, in line with our heart data (Extended Data Figure 11c,d and Supplementary Table 32).

The overall distributions of vascular and stromal cell populations in skeletal and cardiac muscle are similar, including the arterial and venous features of EC, however skeletal muscle contains a single SMC cluster, potentially related to the smaller size of the data set. In skeletal muscle, the predicted cell-cell interactions of the EC_art and SMC include NOTCH1/4-JAG1 as well as JAG1/JAG2/DLL4-NOTCH3, but not JAG1/JAG2/DLL4-NOTCH2, inferred in the heart (Extended Data Figure 11e,f, Supplementary Table 33).

Cardiac Immune cells. Using the logistic regression model, we do not identify any counterpart of the cardiac *IL17RA*+Mo in SKM or kidney, possibly due to the small size of this population.

Naive T cells (CD4+T_naive) identified here express *CCR7* and *SELL*, indicative of their naive and tissue-resident nature⁹⁵. Memory T cells (CD8+T_tem) express *BACH2*, *STAT4* and *IL7R*, associated with long-term immune memory^{96,97}. We further characterised the lymphoid cells using scNym⁹⁸, and train it using data from Stewart B *et al.*, (2019)⁹⁹ and James K *et al.* (2020)¹⁰⁰. The resulting model was applied to our cardiac immune cells and those cells with a predicted score higher than 0.8 were presumed to be likely candidates for re-annotation. Using this approach we identified candidates for Plasma B cells (109), Dendritic cells (645), Innate Lymphoid Cells - ILCs (89), MAIT T cells (219), T helper cells (80) T regulatory cells (11), T central memory cells (103), gamma delta T cells (30) and plasmacytoid dendritic cells (27). These annotations can be found in the cardiac immune object annotations under the label `scNym` at www.heartcellatlas.org.

Reporting summary

Further information on research design is available in the Nature Research Reporting Summary linked to this paper.

Data availability

Data objects with the raw counts matrices and annotation are available via the www.heartcellatlas.org webportal. Raw data are available through the Human Cell Atlas (HCA) Data Coordination Platform (DCP) with accession number: ERP123138 (<https://www.ebi.ac.uk/ena/browser/view/ERP123138>). Source data behind Figures 1b, d, c, 2b, f, 3d, 4b, c and Extended Data Figures 1c, e, 2f, 3b, d, g, l, 4b, c, 5d, 6b, g, 7f, 8e and 9c are available within the manuscript files. The 10X Genomics Visum data for the heart left ventricle tissue can be accessed here: https://support.10xgenomics.com/spatial-gene-expression/datasets/1.1.0/V1_Human_Heart. GWAS data used in this study can be found in Supplementary Table 27.

Code availability

All code used for this study can be accessed as Jupyter notebooks in the project GitHub repository: https://github.com/cartal/HCA_Heart.

68. Ferreira, P. G. *et al.* The effects of death and post-mortem cold ischemia on human tissue transcriptomes. *Nat. Commun.* **9**, 490 (2018).
69. Madissoon, E. *et al.* scRNA-seq assessment of the human lung, spleen, and esophagus tissue stability after cold preservation. *Genome Biol.* **21**, 1 (2019).
70. Litvinukova, M. *et al.* SingleCell and Single Nuclei Analysis Human Heart Tissue v1 (protocols.io.veae3ae). <https://doi.org/10.17504/protocols.io.veae3ae>.
71. Nosedá, M. *et al.* PDGFR α demarcates the cardiogenic clonogenic Sca1+ stem/progenitor cell in adult murine myocardium. *Nat. Commun.* **6**, 6930 (2015).
72. Schindelin, J. *et al.* Fiji: an open-source platform for biological-image analysis. *Nat. Methods* **9**, 676–682 (2012).
73. Wolock, S. L., Lopez, R. & Klein, A. M. Scrublet: Computational Identification of Cell Doublets in Single-Cell Transcriptomic Data. *Cell Syst* **8**, 281–291.e9 (2019).
74. McInnes, L. & Healy, J. UMAP: Uniform Manifold Approximation and Projection for Dimension Reduction. *arXiv [stat.ML]* (2018).
75. Popescu, D.-M. *et al.* Decoding human fetal liver haematopoiesis. *Nature* **574**, 365–371 (2019).
76. Wolf, F. A., Angerer, P. & Theis, F. J. SCANPY: large-scale single-cell gene expression data analysis. *Genome Biol.* **19**, 15 (2018).
77. Luecken, M. D. & Theis, F. J. Current best practices in single-cell RNA-seq analysis: a tutorial. *Mol. Syst. Biol.* **15**, e8746 (2019).
78. Polański, K. *et al.* BBKNN: Fast Batch Alignment of Single Cell Transcriptomes. *Bioinformatics* (2019) <https://doi.org/10.1093/bioinformatics/btz625>.
79. Chen, J., Bardes, E. E., Aronow, B. J. & Jegga, A. G. ToppGene Suite for gene list enrichment analysis and candidate gene prioritization. *Nucleic Acids Res.* **37**, W305–11 (2009).
80. Kuleshov, M. V. *et al.* Enrichr: a comprehensive gene set enrichment analysis web server 2016 update. *Nucleic Acids Res.* **44**, W90–7 (2016).
81. Lotfollahi, M., Wolf, F. A. & Theis, F. J. scGen predicts single-cell perturbation responses. *Nat. Methods* **16**, 715–721 (2019).
82. Miao, Z. *et al.* Putative cell type discovery from single-cell gene expression data. *Nat. Methods* (2020) <https://doi.org/10.1038/s41592-020-0825-9>.

83. Soneson, C. & Robinson, M. D. Bias, robustness and scalability in single-cell differential expression analysis. *Nat. Methods* **15**, 255–261 (2018).
84. La Manno, G. *et al.* RNA velocity of single cells. *Nature* **560**, 494–498 (2018).
85. Bergen, V., Lange, M., Peidli, S., Alexander Wolf, F. & Theis, F. J. Generalizing RNA velocity to transient cell states through dynamical modeling. *bioRxiv* 820936 (2019) <https://doi.org/10.1101/820936>.
86. Traag, V. A., Waltman, L. & van Eck, N. J. From Louvain to Leiden: guaranteeing well-connected communities. *Sci. Rep.* **9**, 5233 (2019).
87. Miragaia, R. J. *et al.* Single-Cell Transcriptomics of Regulatory T Cells Reveals Trajectories of Tissue Adaptation. *Immunity* **50**, 493–504.e7 (2019).
88. Dey, G. *et al.* Signaling network of Oncostatin M pathway. *J. Cell Commun. Signal.* **7**, 103–108 (2013).
89. Abe, H. *et al.* Macrophage hypoxia signaling regulates cardiac fibrosis via Oncostatin M. *Nat. Commun.* **10**, 2824 (2019).
90. Bian, Z. *et al.* Deciphering human macrophage development at single-cell resolution. *Nature* (2020) <https://doi.org/10.1038/s41586-020-2316-7>.
91. Wong, A. P., Nili, N. & Strauss, B. H. In vitro differences between venous and arterial-derived smooth muscle cells: potential modulatory role of decorin. *Cardiovasc. Res.* **65**, 702–710 (2005).
92. Pober, J. S. & Sessa, W. C. Evolving functions of endothelial cells in inflammation. *Nat. Rev. Immunol.* **7**, 803–815 (2007).
93. McDonald, A. I. *et al.* Endothelial Regeneration of Large Vessels Is a Biphasic Process Driven by Local Cells with Distinct Proliferative Capacities. *Cell Stem Cell* **23**, 210–225.e6 (2018).
94. Chen, S.-C., Liu, Y.-C., Shyu, K.-G. & Wang, D. L. Acute hypoxia to endothelial cells induces activating transcription factor 3 (ATF3) expression that is mediated via nitric oxide. *Atherosclerosis* **201**, 281–288 (2008).
95. Hashimoto, K. *et al.* Single-cell transcriptomics reveals expansion of cytotoxic CD4 T cells in supercentenarians. *Proc. Natl. Acad. Sci. U. S. A.* **116**, 24242–24251 (2019).
96. Roychoudhuri, R. *et al.* BACH2 regulates CD8(+) T cell differentiation by controlling access of AP-1 factors to enhancers. *Nat. Immunol.* **17**, 851–860 (2016).
97. Ahrends, T. *et al.* CD4+ T cell help creates memory CD8+ T cells with innate and help-independent recall capacities. *Nat. Commun.* **10**, 5531 (2019).
98. Kimmel, J. C. & Kelley, D. R. scNym: Semi-supervised adversarial neural networks for single cell classification. *bioRxiv* 2020.06.04.132324 (2020) <https://doi.org/10.1101/2020.06.04.132324>.
99. Stewart, B. J. *et al.* Spatiotemporal immune zonation of the human kidney. *Science* **365**, 1461–1466 (2019).
100. James, K. R. *et al.* Distinct microbial and immune niches of the human colon. *Nat. Immunol.* **21**, 343–353 (2020).

Acknowledgements This publication is part of the Human Cell Atlas - www.humancellatlas.org/publications. We gratefully acknowledge the Sanger Flow Cytometry Facility, Sanger Cellular Generation and Phenotyping (CGaP) Core Facility, and Sanger Core Sequencing pipeline for support with sample processing and sequencing library preparation. We gratefully acknowledge the HMS MicRoN Core for their support and assistance in this work. We thank J. Eliasova for graphical images; M. Prete, V. Kiselev and O. Tarkowska for IT support; S. Aldridge for editing the manuscript; C. Dominguez-Conde, J. Park, K. James,

K. Tuong, R. Elmentaite and M. Haniffa for helpful discussions about immune cell annotation, and M. Luecken, M. Lotfollahi, D. Fischer and F. Theis for helpful discussions on computational analyses. We thank T. R. W. Oliver and L. Campos for their assistance with orientation of basic cardiac histology. M.N is the recipient of a British Heart Foundation (BHF) grant (PG/16/47/32156) and JJB is recipient of a BHF grant (FS/13/12/30037,PG/15/57/31580,P G/17/71/33242). M.N, N.H and S.A.T are funded by a BHF/DZHK grant (SP/19/1/34461). N.H is the recipient of an ERC Advanced Grant under the European Union Horizon 2020 Research and Innovation Program (grant agreement AdG788970) and the Federal Ministry of Education and Research of Germany in the framework of CaRNation (031L0075A). N.H, C.E.S, J.G.S are supported by grants from the Leducq Fondation (16CVD03). D.R is supported by the German Research Foundation (DFG). H.Z is supported by the long-term Chinese Council Scholarship (CSC). M.K received funding provided by the Alexander von Humboldt Foundation. H.Z was supported by an EMBO long-term postdoctoral fellowship. G.O received funding provided by the CIHR Canadian Institutes for Health Research, HSF Heart and Stroke Foundation and AI Alberta Innovates. This project has been made possible in part by grant number 2019-202666 from the Chan Zuckerberg Initiative (C.E.S, J.G.S, M.N, N.H and S.A.T). C.T-L, K.P, E.F, E.T, K.R, O.B, H.Z, S.A.T are supported by the Wellcome Sanger Institute grant (WT206194) and the Wellcome Science Strategic Support for a Pilot for the Human Cell Atlas (WT211276/Z/18/Z)). J.G.S and C.E.S are supported by NIH grants (2R01HL080494, 2R01HL080494, 1UM1HL098166). J.G.S and C.E.S. are supported by Engineering Research Centers Program of the National Science Foundation under NSF Cooperative Agreement No. EEC-1647837. C.E.S and B.M. are supported by the Howard Hughes Medical Institute. We are grateful to the deceased donors and their families, the Human Organ Procurement and Exchange Program (HOPE) and to the Cambridge Biorepository for Translational Medicine for access to human tissue.

Author contributions Conceived the study: N.H, S.A.T, M.N, C.E.S, J.G.S, H.M. Acquired tissue: K.M, K.S.P, G.O, H.Z, A.V Processed tissue: M.L, D.R, S.S, E.F, L.T, H.W, J.M.G, B.M, D.M.D, K.R, M.N. Computational methods development: C.T-L, K.P, M.H, J.G.S Cell biology methods development: M.L, E.L.L, M.N, H.M, D.R Histopathological evaluation: J.J.B, M.N Data processing: C.T-L, K.P, G.P Global analysis: C.T-L, D.R, M.L, C.L.W, E.L.L, J.G.S. Cardiomyocyte analysis: D.R, C.L.W, E.N, H.M, N.H, J.G.S, C.E.S. Vascular analysis: M.L, M.N, C.T-L, M.K, S.A.T. Fibroblast analysis: E.L.L, H.M, D.R, M.L, M.K, M.N, J.G.S, C.E.S, N.H. Immune analysis: C.T-L, S.A.T. Neuronal analysis: E.N, D.R, C.L.W, J.G.S, C.E.S. Adipocyte analysis: M.Lee, M.N. Comparative analysis: C.T-L, M.L, M.N, S.A.T. GWAS analysis: M.H, C.T-L, N.H, S.A.T. Interpreted results: M.L, C.T-L, D.R, H.M, C.L.W, E.L.L, M.H, J.B, M.N, C.E.S, J.G.S, S.A.T, N.H. Wrote manuscript: M.L, C.T-L, H.M, D.R, C.L.W, E.L.L, M.K, M.H, J.G.S, C.E.S, M.N, N.H, S.A.T.

Competing interests The authors declare no competing interests.

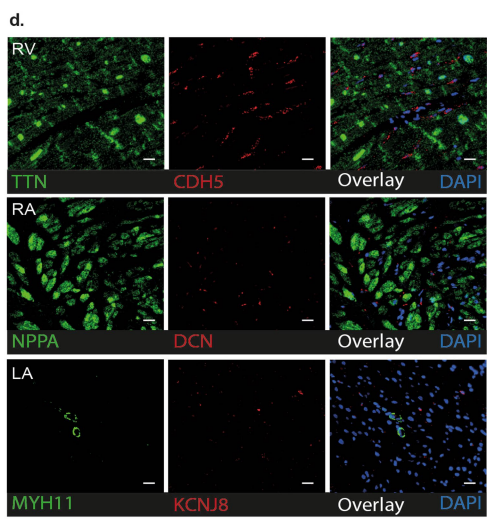
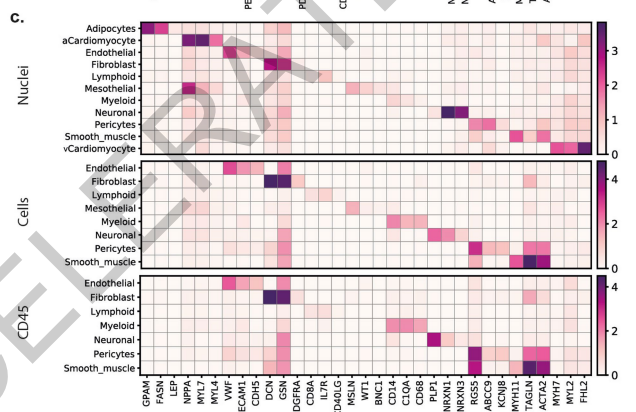
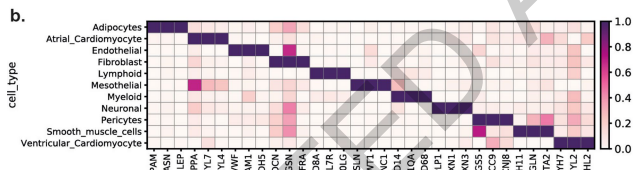
Additional information

Supplementary information is available for this paper at <https://doi.org/10.1038/s41586-020-2797-4>.

Correspondence and requests for materials should be addressed to J.G.S., C.E.S., M.N., N.H. or S.A.T.

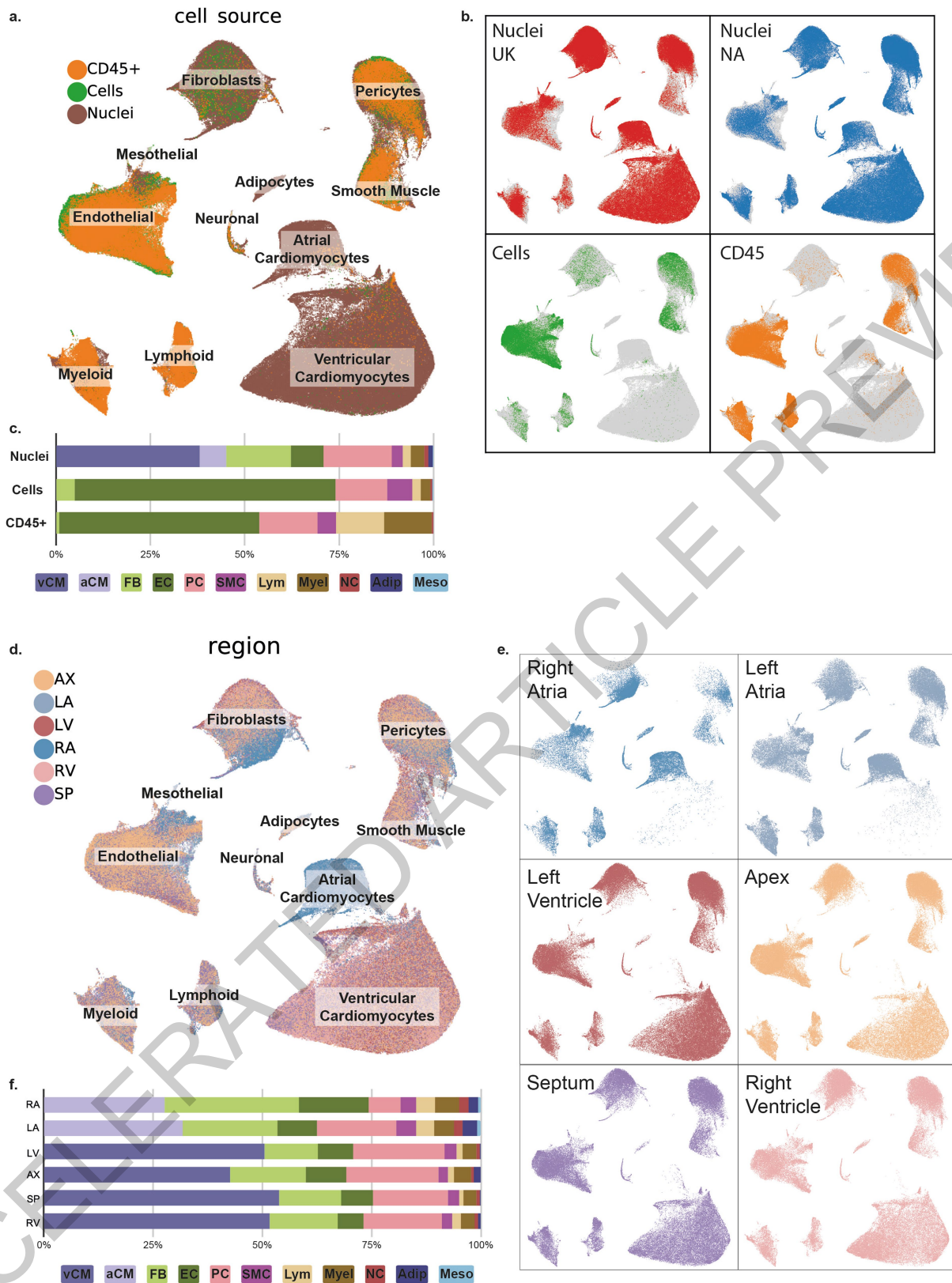
Peer review information *Nature* thanks the anonymous reviewers for their contribution to the peer review of this work. Peer reviewer reports are available.

Reprints and permissions information is available at <http://www.nature.com/reprints>.



Extended Data Fig. 1 | Expression of the canonical markers. a. UMAP embedding of selected canonical markers shown in Figure 1c. **b.** Scaled expression (\log_2FC) of selected canonical markers shown in Figure 1c. **c.** Expression (\log_2FC) of marker genes from Figure 1c in each source highlighting that the same marker genes are used for identification of the same cell types in both cells and nuclei. **d.** Multiplexed smFISH staining of cell type-specific

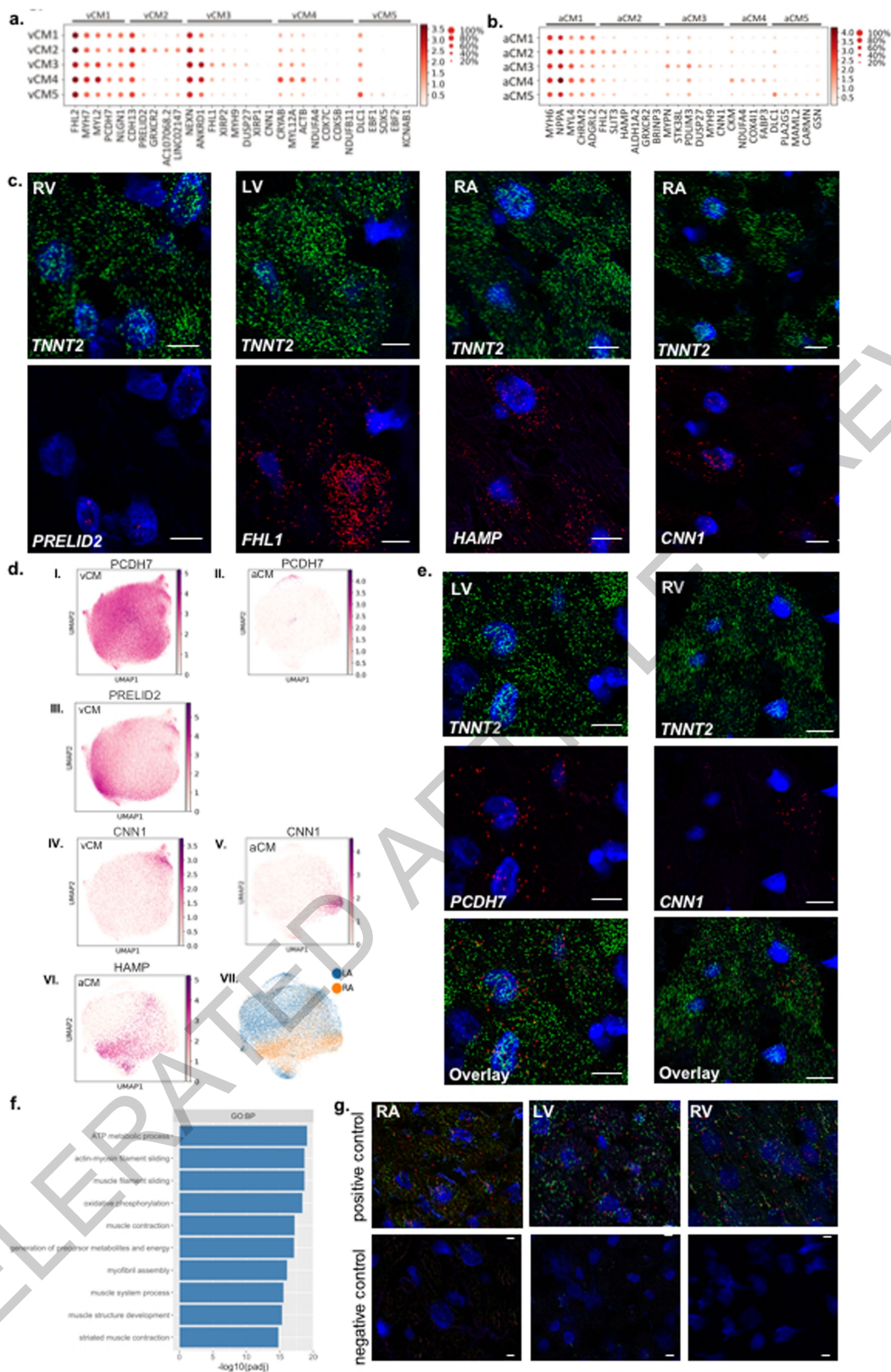
transcripts from Figure 1e in RV (top): *TTN* (green, CM) and *CDH5* (red, EC) RA (middle): *NPPA* (green, aCM) and *DCN* (red, FB) and LA (bottom): *MYH11* (green, SMC) and *KCNJ8* (red, PC), nuclei are DAPI-stained (dark blue). Scale bar 20 μ m. For details on statistics and reproducibility, please see corresponding section in the **Methods**.



Extended Data Fig. 2 | Source and region covariates of the global dataset.

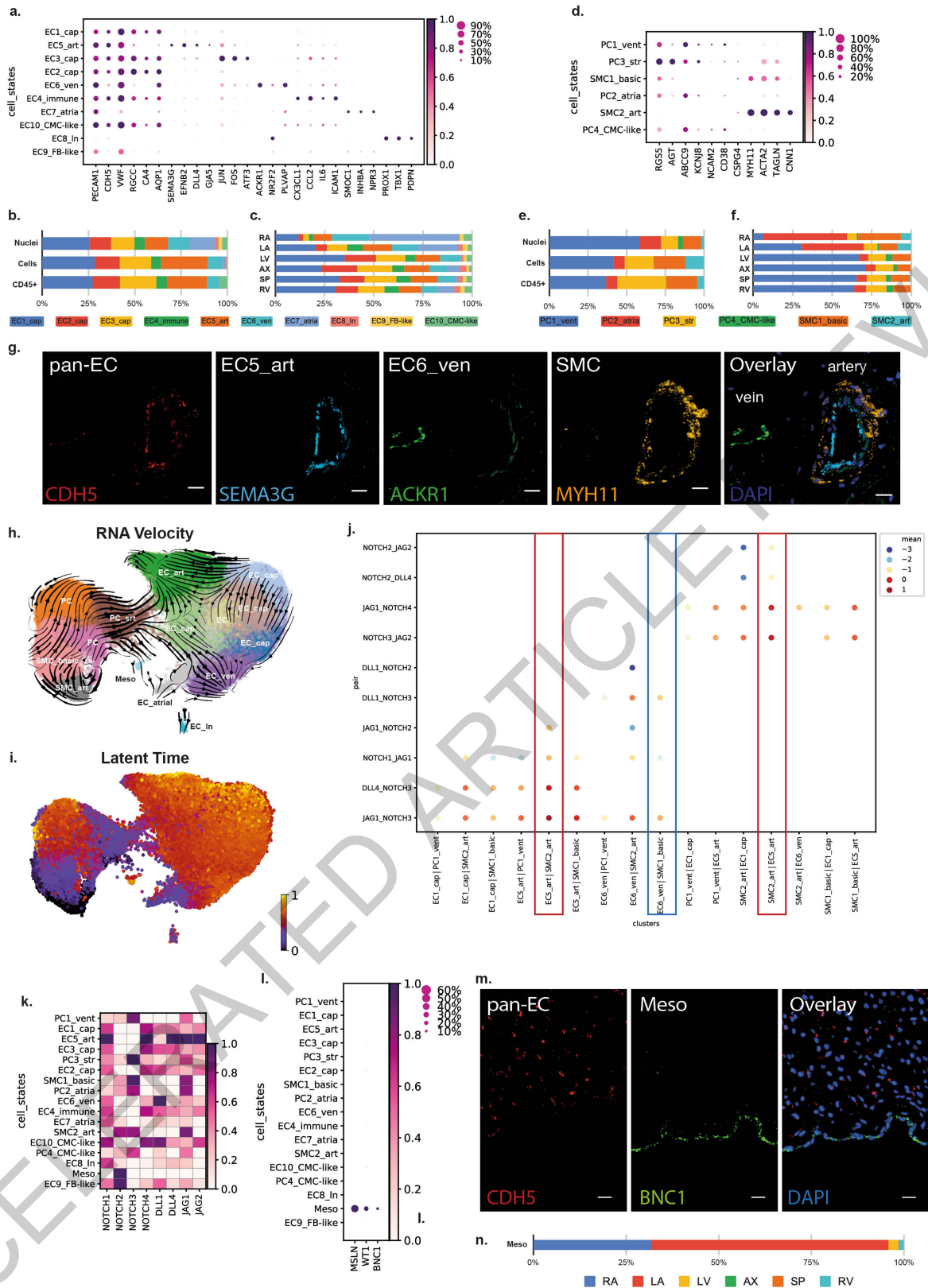
a. UMAP embedding of the major cell types colored by source. **b.** UMAP embedding highlighting the individual sources **c.** Distribution of cell types obtained by each source (Data available in Supplementary Table 29). Further analyses and description available in **Methods** and Supplementary Table 30. **d.**

UMAP embedding of the major cell types colored by region. **e.** UMAP embedding highlighting the individual regions **f.** Distribution of cell types across the six sampled regions (nuclei only) (Data available in Supplementary Table 2).



Extended Data Fig. 3 | Ventricular and atrial cardiomyocytes. **a.** Expression (\log_2FC) of selected marker genes in vCM subpopulations **b.** Expression (\log_2FC) of selected marker genes in aCM subpopulations **c.** Single channel multiplexed smFISH images of overlay shown in Figure 2c, d, g, and h. **d.** Expression (\log_2FC) of specific markers in cardiomyocyte subpopulations: I and II. show *PCDH7* expression in vCM and aCM respectively. III. *PRELID2* expression is highest in vCM2 and is enriched in RV. IV and V. *CNN1* expression is enriched in both vCM3 and aCM3. VI and VII. *HAMP* expression is enriched in RA

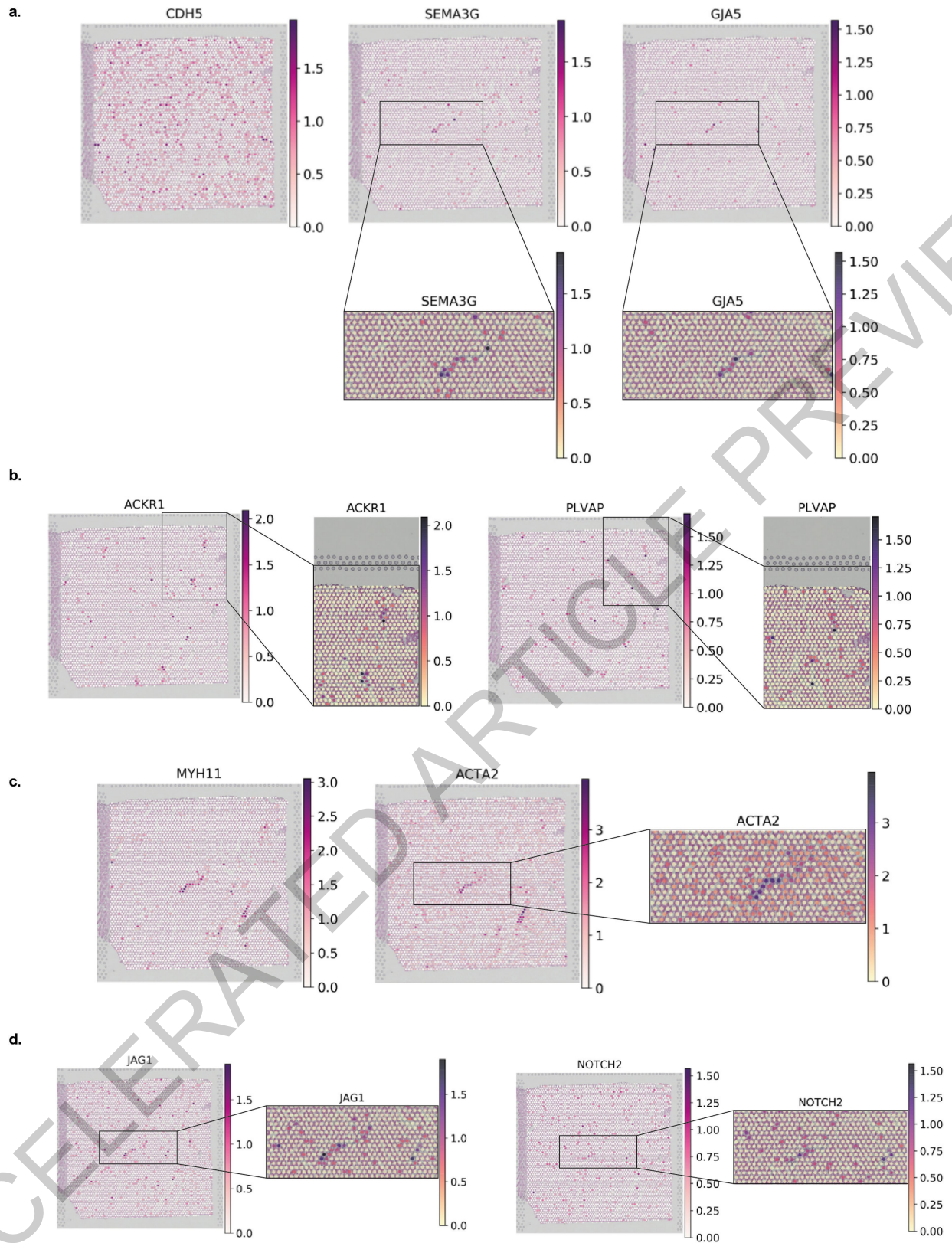
e. Multiplexed smFISH of transcripts enriched in CM subpopulations: Left: expression of *TNNT2* (green) and *PCDH7* (red) in LV. Right: expression of *TNNT2* (green) and *CNN1* (red) in RV, nuclei are DAPI-stained (dark blue). Scale bar 10 μm . **f.** Gene Ontology analysis results for vCM4 showing significant terms related to energy metabolism and muscle contraction (Data available in Supplementary Table 6). **g.** Multiplexed smFISH of positive and negative RNAscope control probes. Scale bar 5 μm . For details on statistics and reproducibility, please see corresponding section in the **Methods**.



Extended Data Fig. 4 | See next page for caption.

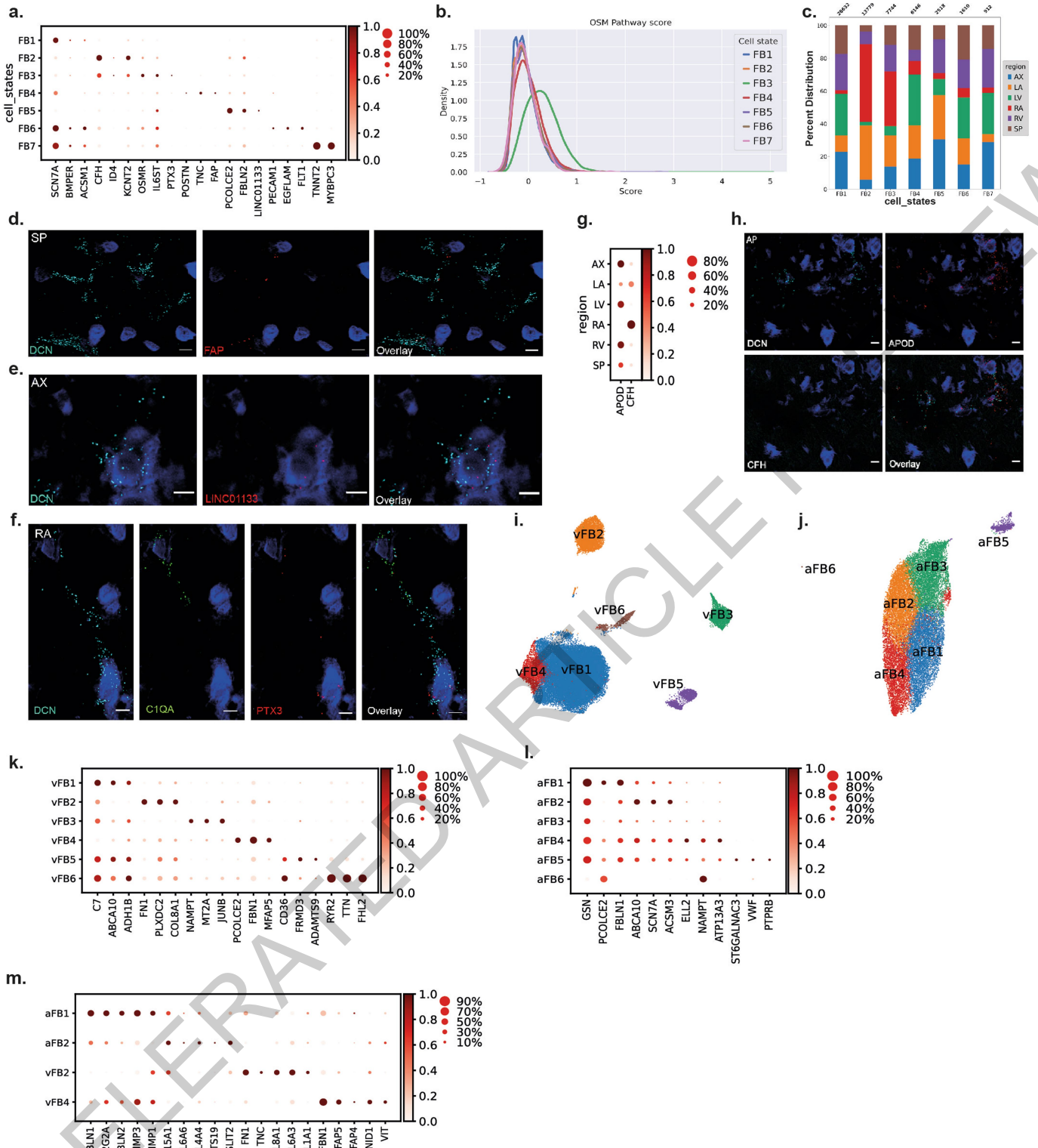
Extended Data Fig. 4 | Vascular and mesothelial populations. **a.** Scaled expression (\log_2FC) of selected marker genes for EC subpopulations. Distribution of the EC subpopulations across **b.** the sources and **c.** the regions (nuclei only) (Data available in Supplementary Table 9). **d.** Scaled expression (\log_2FC) of selected marker genes of pericytes and smooth muscle cell subpopulations. Distribution of the mural subpopulations across **e.** the sources and **f.** the regions (nuclei only) (Data available in Supplementary Table 9). **g.** Multiplexed smFISH in AX section shows *MYH11* (yellow) expression in vascular SMC (thick in artery and very thin in nearby small caliber vein), *CDH5* (red) in the endothelium, and *SEMA3G* (cyan) and *ACKR1* (green) expression respectively in arterial and venous EC, nuclei are DAPI-stained (dark blue). Scale bar 20 μm . **h.** UMAP embedding of vascular and mesothelial cells with stochastic representation of the RNA velocity and **i.** latent time of the vascular cells showing predicted directionalities of the cell populations based on the RNA splicing dynamics. The analysis uses only cells, nuclei are omitted. (EC_cap = capillary endothelial cells, EC_art = arterial endothelial cells, EC_ven = venous endothelial cells, EC_atrial = atrial endothelial cells, EC_In = lymphatic endothelial cells, PC = pericytes, PC_str = stromal pericytes, SMC_basic = smooth muscle cells, SMC_art = arterial smooth muscle cells, Meso = mesothelial cells). **j.** Predicted cell-cell interactions using the CellphoneDB

statistical inference framework on 39 000 cells from 14 biologically independent individuals ($n = 14$). Selected ligand-receptor interactions show specificity of NOTCH ligands-receptors pairing in defined vasculature beds. **Mean:** Mean of combined gene expression of interacting pairs (\log_2FC). CellPhoneDB p -value of the specificity of the interactions = $10e^{-5}$. The red rectangles highlight the arterial interactions and the blue rectangle highlights venous interactions depicted in Figure 3d. Notably, even though the EC6_ven and SMC2_art interaction is unexpected, we can't exclude that those cell states are restricted to their respective vascular beds. Further validation is needed to determine the exact spatial distribution of EC6_ven and SMC2_art and subsequently verify whether the interaction is plausible in vivo (Data available in Supplementary Table 10). **k.** Scaled expression (\log_2FC) of the ligands and receptors from **g.** across the vascular populations described in Figure 3a. **l.** Scaled expression (\log_2FC) of selected marker genes of mesothelial cells. **m.** Multiplexed smFISH localises the mesothelial cells expressing *BNC1* into the epicardium of the left atria. *CDH5* shows endothelial cells in the tissue and is absent from the mesothelial cells, nuclei are DAPI-stained (dark blue). Scale bar 20 μm . **n.** Distribution of the mural subpopulations across the sampled regions (nuclei only) (Data available in Supplementary Table 9). For details on statistics and reproducibility, please see corresponding section in the **Methods**.



Extended Data Fig. 5 | Vascular markers visualized on 10X Genomics Visium data. Spatial expression (\log_2FC) of **a.** *CDH5* (pan-EC marker), *SEMA3G* and *GJA5* (arterial EC markers), **b.** *ACKR1* and *PLVAP* (venous EC markers), **c.** *MYH11* and

ACTA2 (pan-SMC markers), **d.** *JAG1* and *NOTCH2* on publicly available 10X Visium section of human left ventricle. *JAG1* and *NOTCH2* are the predicted interaction partners for arterial EC and SMC respectively.



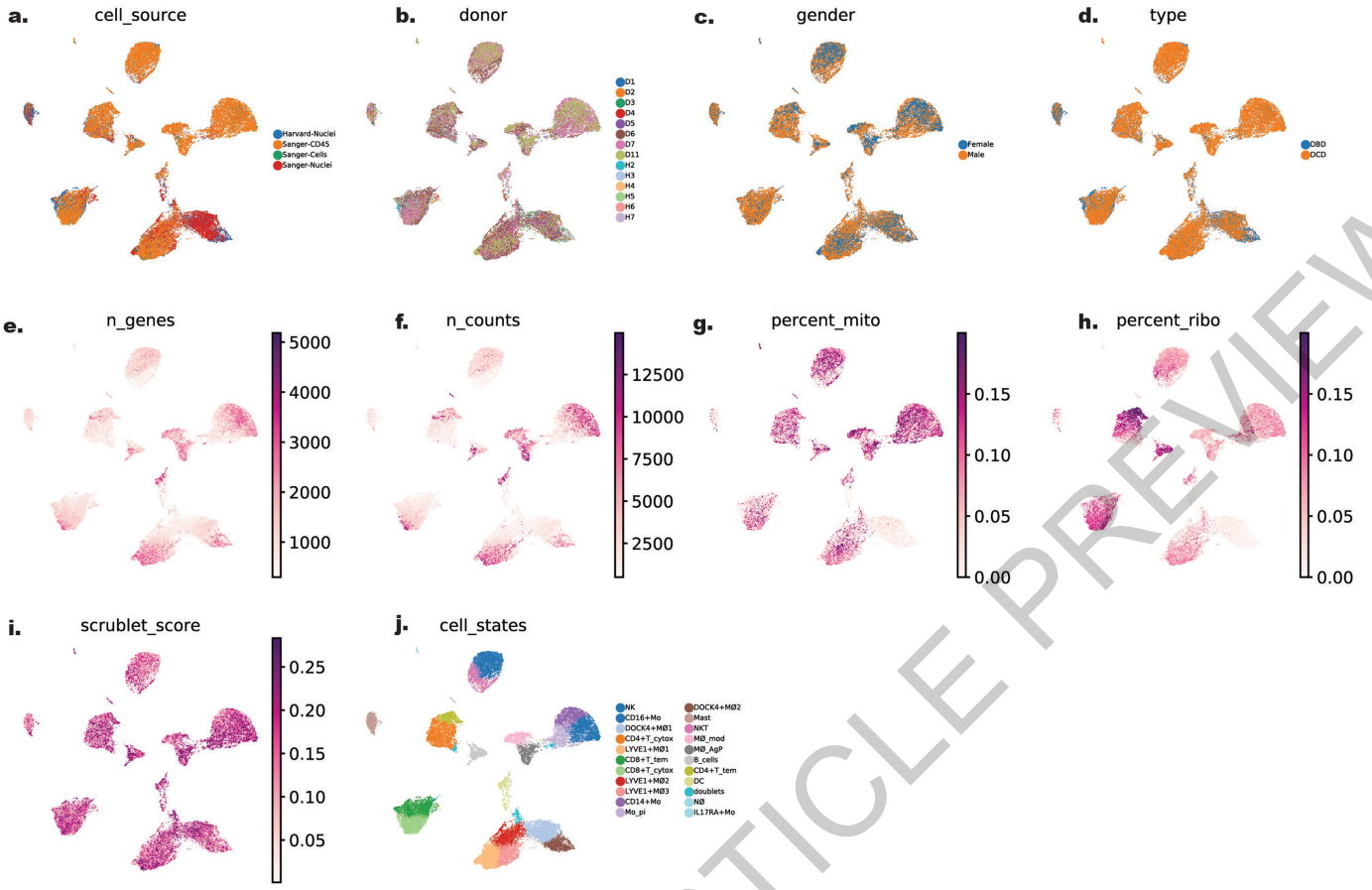
Extended Data Fig. 6 | See next page for caption.

Article

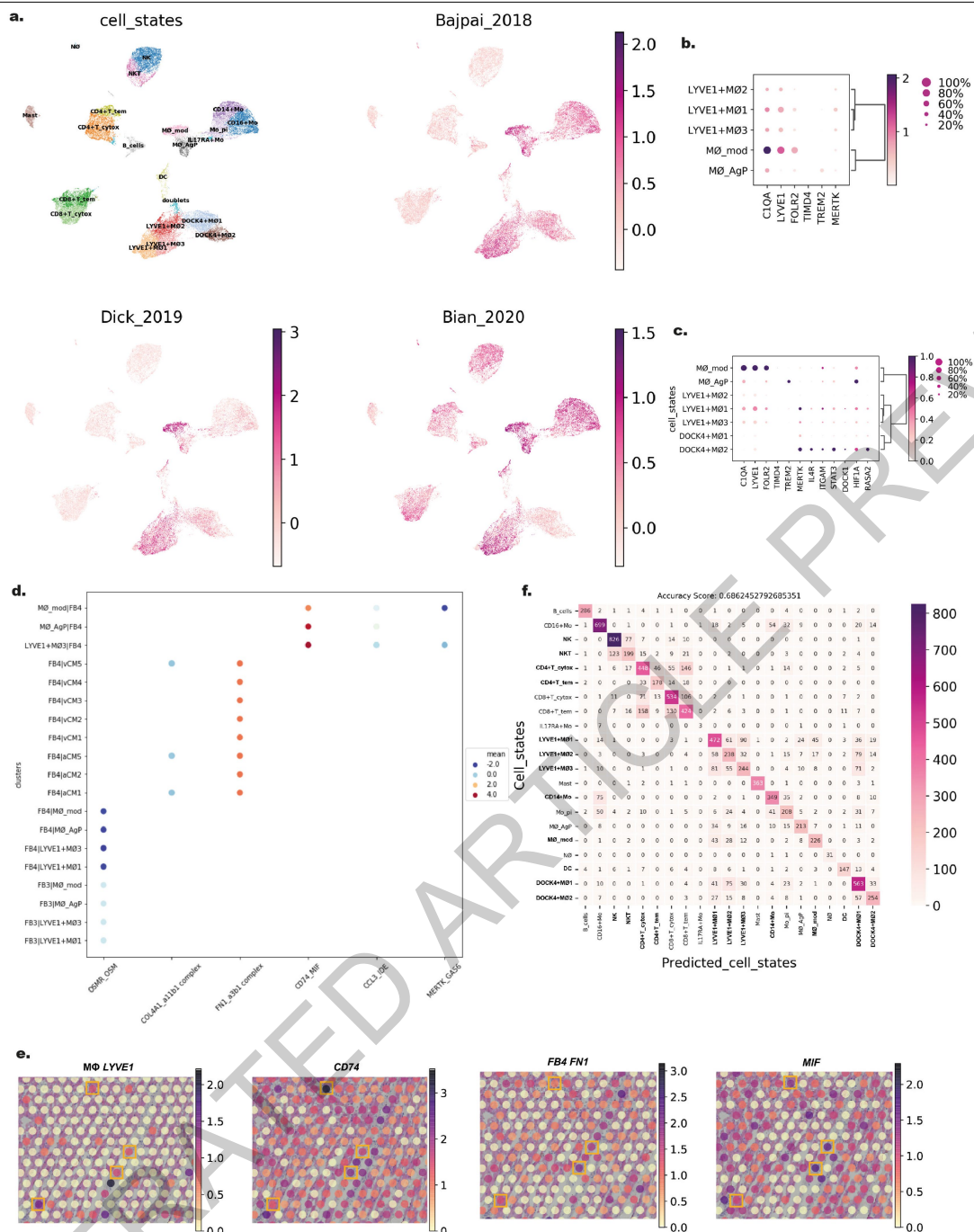
Extended Data Fig. 6 | Fibroblasts. **a.** Scaled expression (\log_2FC) of selected marker genes of identified FB populations. **b.** Enrichment for Oncostatin M pathway for FB populations showing enriched activity in FB3. A list of genes with which the score was calculated available in Supplementary Table 12. **c.** Regional distribution per FB population. Some FB populations show enrichment in the atria (RA, LA), such as FB2 and FB3. FB1, FB4-6 is enriched in the ventricles (LV, RV, AX and SP) (Data available in Supplementary Table 35). **d., e., f.** Multiplexed smFISH for probes targeting *FAP*, *LINC01133* and *PTX3* confirming FB4, FB5 and FB3 subpopulations. *FAP* (red) is imaged in SP, *LINC01133* (red) in AX and *PTX3* (red) in RA tissue section. *DCN* (cyan) is used as a pan-FB marker, *CIQA* (green) as a pan-macrophage marker, nuclei are DAPI-stained (dark blue). Scale bar 5 μ m. **g.** Scaled expression (\log_2FC) of *APOD* and

CFH genes, which represent differences between ventricular and atrial fibroblasts. **h.** Multiplexed smFISH of AX section representing *DCN* (cyan), *APOD* (red) and *CFH* (green), nuclei are DAPI-stained (dark blue). While *APOD* signal colocalized with *DCN*, expression of *CFH* was absent. Scale bar 5 μ m. **i.** UMAP embedding of the ventricular fibroblast cell-states. **j.** UMAP embedding of atrial fibroblasts cell types **k.** Scaled expression (\log_2FC) of marker genes for ventricular fibroblast subpopulations. **l.** Scaled expression (\log_2FC) of marker genes for atrial fibroblast subpopulations **m.** Scaled expression (\log_2FC) of ECM genes differentiating atrial (aFB1, aFB2) and ventricular (vFB2, vFB4) clusters which suggest different ECM mechanisms. For details on statistics and reproducibility, please see corresponding section in the **Methods**.

ACCELERATED ARTICLE PREVIEW

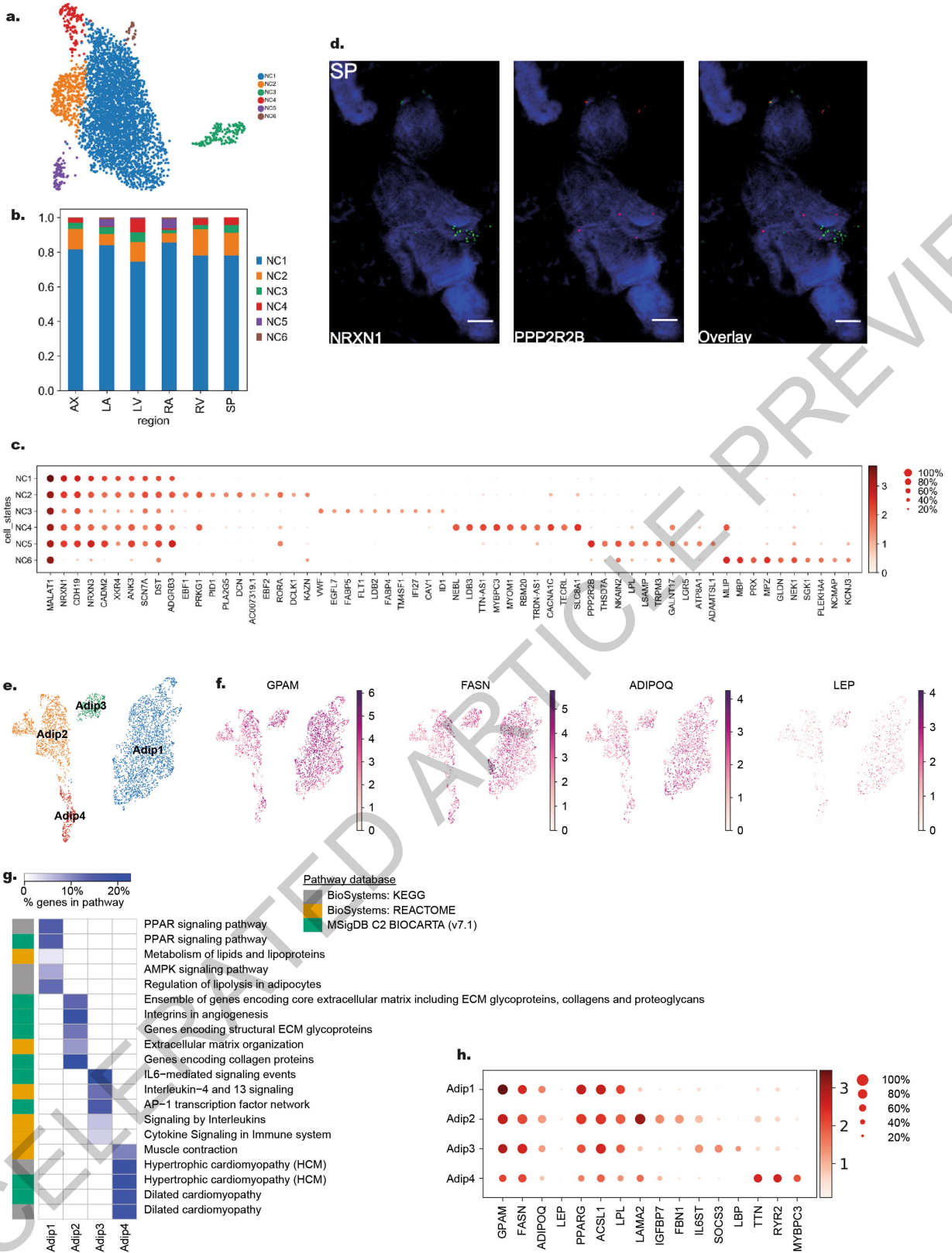


Extended Data Fig. 7 | Covariates of immune cardiac populations. UMAP embedding of **a.** cell source, **b.** donor, **c.** gender, **d.** type, **e.** number of genes, **f.** number of counts, **g.** percentage of mitochondrial genes, **h.** percentage of ribosomal genes, **i.** scrublet score and **j.** annotation of the cell populations of the immune cells.



Extended Data Fig. 8 | Immune cardiac populations. **a.** Visualisation of transcriptional signatures from published studies. The score values represent the likelihood of the external transcriptional signature to be present when comparing it against the transcriptional background of a cardiac immune population. **Bajpai_2018** = *CCR2-MERTK*+ Tissue resident macrophages from Bajpai *et al* 2018., **Dick_2019** = Self renewing tissue macrophages from Dick SA *et al* 2019, **Bian_2020** = Yolk sac-derived macrophages from Bian Z *et al* 2020. The complete signature can be found in Supplementary Table 19. **b.** Expression (\log_2FC) of *LYVE1*, *FOLR2* and *TIMD4* characteristic of the self-renewing tissue-resident murine macrophages described in Dick SA *et al* 2019, as well as *MERTK* as described in Bajpai *et al* 2018 and the *TIMD2* expression associated to Lipid-Associated MΦ (LAM) described in Jaitin D *et al* 2019. Complete signatures can be found in Supplementary Table 19. **c.** Scaled

expression (\log_2FC) of genes differentiating *DOCK4+M01* from *DOCK4+M02*: *IL4R*, *ITGAM*, *STAT3*, *DOCK1*, *HIF1A*, *RASA2*. **d.** Predicted cell-cell interactions calculated for 69 295 cardiomyocytes, fibroblasts and myeloid cells from 14 donors (n = 14) and enriched for “Extracellular matrix organisation”. **Mean:** Mean of combined gene expression of interacting pairs (\log_2FC). (Data available in Supplementary Table 17). **e.** Spatial mapping of the *CD74_MIF* interaction between *LYVE1+MΦ* and *FB4* on a publicly available 10X Genomics Visium dataset for LV myocardium. We identified four spots where we observe co-expression of *FN1*, *LYVE1*, *CD74* and *MIF*, as predicted from the cell-cell interactions. The bar represents the \log_2FC . **f.** Confusion matrix for the logistic regression model trained on cardiac immune cells. This model reached an accuracy score of 0.6862, showing a stronger accuracy with lymphoid cells, compared with the myeloid ones.



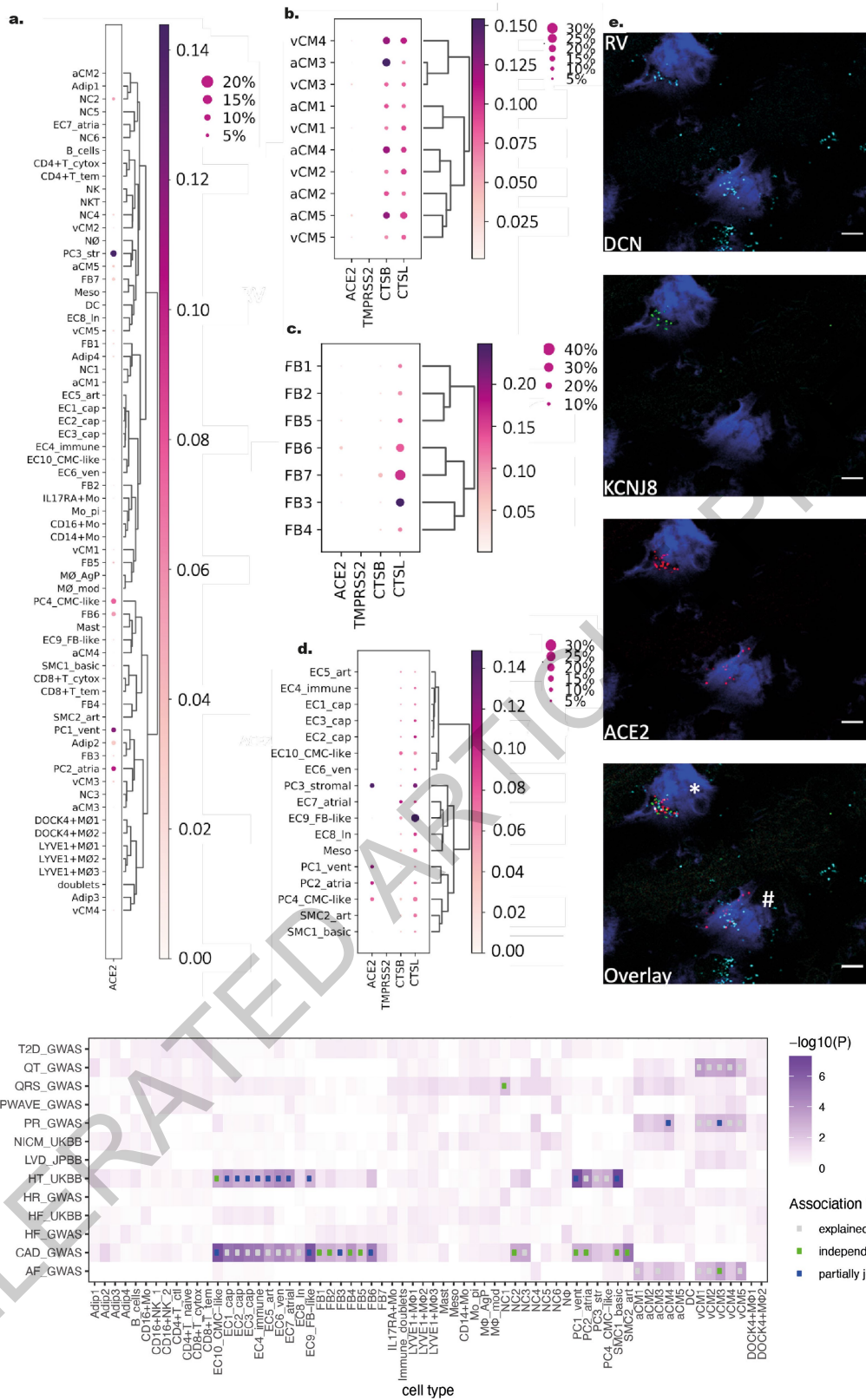
Extended Data Fig. 9 | See next page for caption.

Article

Extended Data Fig. 9 | Neuronal and adipocyte populations. **a.** UMAP embedding identifies six neuronal subpopulations. **b.** Regional distribution of NC subpopulations identified in **a** (Data available in Supplementary Table 20). **c.** Expression (\log_2FC) dotplot of selected marker genes in NC subpopulations. **d.** Multiplexed smFISH of *NRXNI* (green) and *PPP2R2B* (red), nuclei were DAPI-stained (dark blue). Scale bar 5 μ m. For details on statistics and reproducibility, please see corresponding section in the **Methods**. **e.** UMAP embedding showing four adipocyte subpopulations. **f.** UMAP embedding of expression of

gene markers associated with adipocytes (*GPAM*, *FASN*, *ADIPOQ*, *LEP*). **g.** Top 5 significantly enriched pathways for each adipocyte subpopulation, using differentially expressed genes calculated using the Wilcoxon Rank Sum test with Benjamini-Hochberg correction ($\log_2FC > 0.5$, p -value $< 1.0e-05$) and tested using a hypergeometric distribution with Bonferroni correction as implemented in ToppFun (Data available in Supplementary Table 21). **h.** Expression (\log_2FC) of adipocyte associated genes and select marker genes from the top enriched pathway for each adipocyte subpopulation.

ACCELERATED ARTICLE PREVIEW



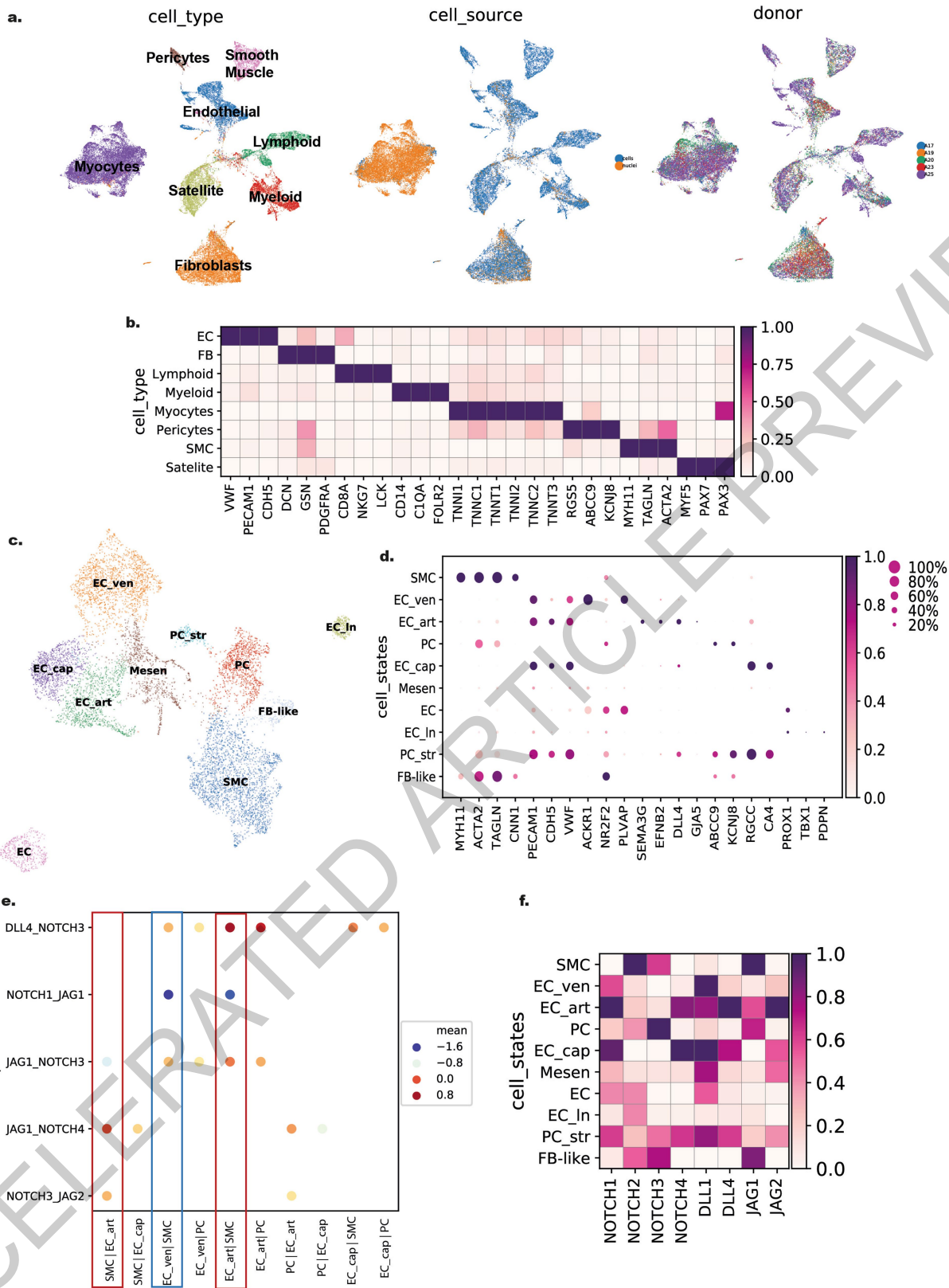
Extended Data Fig. 10 | See next page for caption.

Article

Extended Data Fig. 10 | Relevance for COVID-19 and GWAS studies. **a.** Global expression (\log_2FC) of *ACE2* in all cardiac cells. Gene expression of *ACE2*, *TMPRSS2*, *CTSB* and *CTSL* in **b.** Cardiomyocytes, **c.** Fibroblasts and **d.** Vascular cells. **e.** Multiplexed smFISH expression of *DCN* (cyan), *KCNJ8* (green) and *ACE2* (red), nuclei are DAPI-stained (dark blue) marking fibroblasts (#; expression of *DCN*) and pericytes (*; co-expression of *DCN* and *KCNJ8*) in RV tissue section. Scale bar 5 μ m. For details on statistics and reproducibility, please see corresponding section in the **Methods**. **f.** The color coding of the heatmap shows the $-\log_{10}(P\text{-value})$ of the MAGMA GWAS enrichment analysis for the association between cell type specific expression (y-axis) and GWAS signals

(x-axis). The cell types refer to the subcluster annotations and GWAS studies refer to Supplementary table H (AF: atrial fibrillation, CAD: coronary artery disease, HF: heart failure, HR: heart rate, HT: hypertension, LVD: left ventricular diameter, NICM: non ischemic cardiomyopathy, PR: PR interval, PWAVE: P-wave duration, QRS: QRS complex duration, QT: QT interval, T2D: type 2 diabetes). Dots mark significant associations (FDR < 10%). The color of the dots indicates the type of association as determined by pairwise conditional analysis (green: independent association, blue: partially jointly explained with other cell types, grey: explained away by other cell types) (Data available in Supplementary Table 28).

ACCELERATED ARTICLE PREVIEW



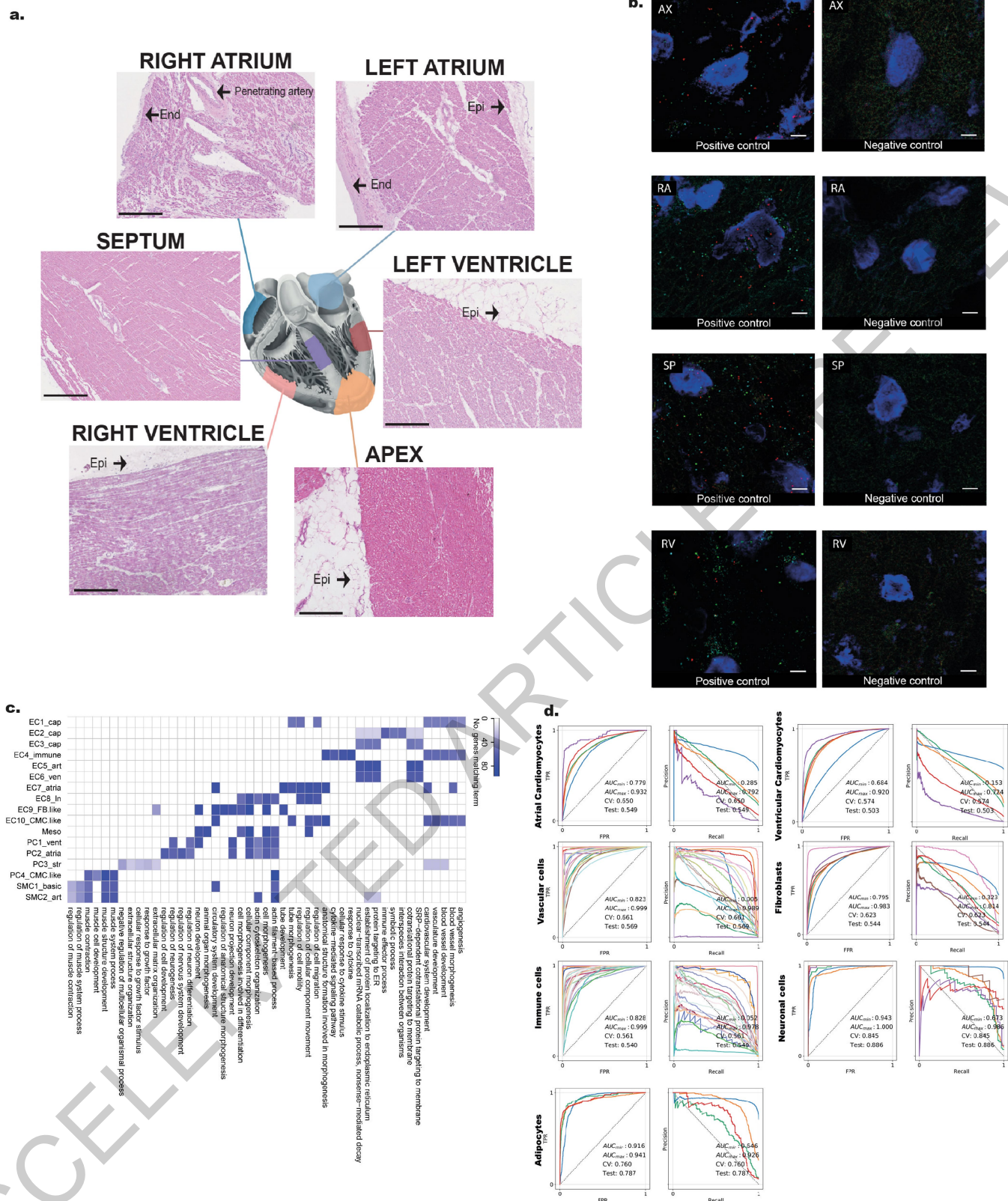
Extended Data Fig. 11 | See next page for caption.

Article

Extended Data Fig. 11 | Skeletal muscle populations. **a.** UMAP embedding of transcriptional data from skeletal muscle using cells and nuclei. (EC = endothelial cells, FB = Fibroblasts, Mural = pericytes and smooth muscle cells). **b.** Scaled expression (\log_2FC) of selected markers for the major skeletal muscle populations. **c.** UMAP embedding of vascular and stromal populations of skeletal muscle (EC = endothelial cells, SMC = smooth muscle cells, EC_art = arterial endothelial cells, EC_ven = venous endothelial cells). **d.** Scaled expression (\log_2FC) of marker genes used in Extended Data Figure 3 for identification of vascular cell states. **e.** Predicted cell-cell interactions inferred using CellPhoneDB statistical inference framework in skeletal muscle cells with

9 220 cells from five donors (n = 5) depicting cell states from **c.** Selected ligand-receptor interactions show specificity of NOTCH ligands-receptors pairing in defined vasculature beds. The interactions of EC_art-SMC are highlighted by a red rectangle and EC_ven-SMC are highlighted by a blue rectangle. Color of the dots indicates the mean expression level of interacting molecule in partner 1 and interacting molecule partner 2. **Mean:** Mean of combined gene expression of interacting pairs (\log_2FC). CellPhoneDB *p*-value of the specificity of the interactions = $10e-5$ (Data available in Supplementary Table 10). **f.** Scaled expression (\log_2FC) of the ligands and receptors from Extended Data Figure 3 depicted on vascular populations of skeletal muscle.

ACCELERATED ARTICLE PREVIEW



Extended Data Fig. 12 | Analysis technical information. **a.** Locations and representative histology section of six cardiac regions sampled, including right atrium (RA), left atrium (LA), right ventricular free wall (RV), left ventricular free wall (LV) and left ventricular apex (AX) and interventricular septum (SP). H&E, magnification $\times 10$, bar=500 μm . **b.** Spatial visualization of positive and negative RNA scope control probes. Scale bar 5 μm . For details on statistics and reproducibility, please see corresponding section in the **Methods**. **c.** Heatmap of top 5 significantly enriched Gene Ontology Biological

Processes term for each of the vascular subpopulations from Figure 3a (Data available in Supplementary Table 25). **d.** SCAF scores for each batch aligned manifold. For each population we plot the True Positive (TPR) versus False Positive (FPR) learning ratios from the subpopulation in each manifold. Next we plot how accurately the manifold represents each learned subpopulation based on the **Test** training set and the CV cross-validation set. The closer the CV value to the Test value, the better the manifold is at representing the subpopulations.

Reporting Summary

Nature Research wishes to improve the reproducibility of the work that we publish. This form provides structure for consistency and transparency in reporting. For further information on Nature Research policies, see our [Editorial Policies](#) and the [Editorial Policy Checklist](#).

Statistics

For all statistical analyses, confirm that the following items are present in the figure legend, table legend, main text, or Methods section.

- | n/a | Confirmed |
|-------------------------------------|--|
| <input type="checkbox"/> | <input checked="" type="checkbox"/> The exact sample size (n) for each experimental group/condition, given as a discrete number and unit of measurement |
| <input type="checkbox"/> | <input checked="" type="checkbox"/> A statement on whether measurements were taken from distinct samples or whether the same sample was measured repeatedly |
| <input type="checkbox"/> | <input checked="" type="checkbox"/> The statistical test(s) used AND whether they are one- or two-sided
<i>Only common tests should be described solely by name; describe more complex techniques in the Methods section.</i> |
| <input type="checkbox"/> | <input checked="" type="checkbox"/> A description of all covariates tested |
| <input type="checkbox"/> | <input checked="" type="checkbox"/> A description of any assumptions or corrections, such as tests of normality and adjustment for multiple comparisons |
| <input type="checkbox"/> | <input checked="" type="checkbox"/> A full description of the statistical parameters including central tendency (e.g. means) or other basic estimates (e.g. regression coefficient) AND variation (e.g. standard deviation) or associated estimates of uncertainty (e.g. confidence intervals) |
| <input type="checkbox"/> | <input checked="" type="checkbox"/> For null hypothesis testing, the test statistic (e.g. F , t , r) with confidence intervals, effect sizes, degrees of freedom and P value noted
<i>Give P values as exact values whenever suitable.</i> |
| <input checked="" type="checkbox"/> | <input type="checkbox"/> For Bayesian analysis, information on the choice of priors and Markov chain Monte Carlo settings |
| <input checked="" type="checkbox"/> | <input type="checkbox"/> For hierarchical and complex designs, identification of the appropriate level for tests and full reporting of outcomes |
| <input checked="" type="checkbox"/> | <input type="checkbox"/> Estimates of effect sizes (e.g. Cohen's d , Pearson's r), indicating how they were calculated |

Our web collection on [statistics for biologists](#) contains articles on many of the points above.

Software and code

Policy information about [availability of computer code](#)

Data collection	Software used include: BD FACS Software 1.2.0.142 (BD Influx), Summit V5.4.0.16584 (BD XDP), BD FACSDIVA 6.1.3 (Aria), Axiovision 4.9.1 and ZEN 2.3 software (Zeiss), Harmony 4.9 (Perkin Elmer), Chromium Controller Firmware version 5.00 (10X Genomics).
Data analysis	Software used include: R 3.6, Python 3.7, 10X Genomics' Cell Ranger 3.0.2, Harmony 4.9 (Perkin Elmer), Axiovision 4.9.1 and ZEN 2.3 (Zeiss), Adobe Illustrator 24.2.3, CorelDraw X4, 10X Genomics' Space Ranger 1.0.0, ImageJ 1.52Q or 1.52P, Scanpy 1.4, bbknn 1.3.11, scGen 6c237d7, anndata 1.7, pandas 1.0.1, numpy 1.19, scVelo 1d87464.

For manuscripts utilizing custom algorithms or software that are central to the research but not yet described in published literature, software must be made available to editors and reviewers. We strongly encourage code deposition in a community repository (e.g. GitHub). See the Nature Research [guidelines for submitting code & software](#) for further information.

Data

Policy information about [availability of data](#)

All manuscripts must include a [data availability statement](#). This statement should provide the following information, where applicable:

- Accession codes, unique identifiers, or web links for publicly available datasets
- A list of figures that have associated raw data
- A description of any restrictions on data availability

The data is made available through the Human Cell Atlas (HCA) Data Coordination Platform (DCP) and can be accessed here: <https://www.ebi.ac.uk/ena/browser/view/ERP123138>. The data can also be accessed and explored through the HCA Heart Project website at www.heartcellatlas.org.

Field-specific reporting

Please select the one below that is the best fit for your research. If you are not sure, read the appropriate sections before making your selection.

Life sciences Behavioural & social sciences Ecological, evolutionary & environmental sciences

For a reference copy of the document with all sections, see [nature.com/documents/nr-reporting-summary-flat.pdf](https://www.nature.com/documents/nr-reporting-summary-flat.pdf)

Life sciences study design

All studies must disclose on these points even when the disclosure is negative.

Sample size	No sample-size calculation was done due to the nature of this study. Non-failing hearts were collected from human donors from July 2018 to July 2019 on the basis of availability from CBTM (Cambridge, UK) and The University of Alberta (Canada). Our study explores the cellular composition of the healthy adult human heart and we state that the number of samples is not enough to make generalisations.
Data exclusions	No data were excluded from the analysis. For the final count matrix, we excluded cells based on pre-established criteria for single-cells: we excluded low quality samples and contaminating cells (i.e. - cells with low number of detected genes and high mitochondria content).
Replication	We performed single nuclei RNAseq on 14 hearts (4 - 6 regions each) and single cell RNAseq on 7 hearts (4 - 6 regions each), with comparable results among all the donors. The same samples were used for the validation experiments. The micrographs in Figure 2g, 3c/h and Extended Data Figure 2c (HAMP), 2e (CNN1), 3f, 3k, 4f are repeated with similar results in 2 individual tissue sections. The micrographs in Figure 2h, 3f and Extended Data Figure 2c (CNN1), 2e (PCDH7), 4e, 4h, 6d are repeated with similar results in 3 individual tissue sections. The micrographs in Figure 1e, 2d, 3e, and Extended Data Figure 1f, 2c (FHL1) and 4d are repeated with similar results in 4 individual tissue sections. The micrographs in Figure 2c and Extended Data Figure 2c (PRELID2), 7e, 9a are repeated with similar results in 6 or more individual tissue sections. Positive and negative controls were done once per used samples. For skeletal muscle analysis, single cells and single nuclei were isolated from 5 individuals, with comparable results among all the donors.
Randomization	Only healthy individuals were considered in our analysis. Randomisation was not relevant due to the study design where non-failing hearts were used on availability.
Blinding	Only healthy individuals were considered in our analysis. Blinding was not relevant due to the study design where non-failing hearts were used on availability, and the analytical strategy would not benefit from it.

Reporting for specific materials, systems and methods

We require information from authors about some types of materials, experimental systems and methods used in many studies. Here, indicate whether each material, system or method listed is relevant to your study. If you are not sure if a list item applies to your research, read the appropriate section before selecting a response.

Materials & experimental systems

n/a	Involved in the study
<input type="checkbox"/>	<input checked="" type="checkbox"/> Antibodies
<input checked="" type="checkbox"/>	<input type="checkbox"/> Eukaryotic cell lines
<input checked="" type="checkbox"/>	<input type="checkbox"/> Palaeontology and archaeology
<input checked="" type="checkbox"/>	<input type="checkbox"/> Animals and other organisms
<input type="checkbox"/>	<input checked="" type="checkbox"/> Human research participants
<input checked="" type="checkbox"/>	<input type="checkbox"/> Clinical data
<input checked="" type="checkbox"/>	<input type="checkbox"/> Dual use research of concern

Methods

n/a	Involved in the study
<input checked="" type="checkbox"/>	<input type="checkbox"/> ChIP-seq
<input type="checkbox"/>	<input checked="" type="checkbox"/> Flow cytometry
<input checked="" type="checkbox"/>	<input type="checkbox"/> MRI-based neuroimaging

Antibodies

Antibodies used	anti-human CD45 monoclonal antibody-conjugated microbeads (Miltenyi Biotec, 130-045-801) in dilution 1:4 (20 ul of antibody-labeled microbeads in 80 ul of cell suspension buffer).
Validation	Commercially available product, full protocol and validation available at miltenyibiotec.com/_Resources/Persistent/25cf8ecca93dc183f1d96d5348e58ca0e9a07c40/DS130-045-801.pdf

Human research participants

Policy information about [studies involving human research participants](#)

Population characteristics	Tissues were obtained from 14 individuals, eight (D1-7 and 11) collected in the United Kingdom and six (H2-7) collected in
----------------------------	--

Population characteristics	North America. The cohort consisted of seven male (D2, D3, D6, D7, H2, H3 and H4) and seven female (D1, D4, D5, D11, H5, H6 and H7) donors, in the range of 40-75 years of age. Six of the donors were classified as DCD (Donation after Circulatory Death, D2, D4-7 and D11) and eight donors were classified as DBD (Donation after Brain Death, D1, D3, H2-7).
Recruitment	Cardiovascular history was unremarkable for all donors, and this was the main recruitment criteria used for to include individuals in our study. We believe this method of recruitment does not represent any bias that can impact our results.
Ethics oversight	Heart tissues (D1-7 and 11) were obtained from deceased transplant organ donors after Research Ethics Committee approval (Ref 15/EE/0152, East of England - Cambridge South Research Ethics Committee) and informed consent from the donor families. Heart tissues (H2-7) were obtained from deceased organ donors after Human Research Ethics Board approval Pro00011739 (University of Alberta, Edmonton, Canada). Informed consent from donor families was acquired via the institutional Human Organ Procurement and Exchange Program (HOPE).

Note that full information on the approval of the study protocol must also be provided in the manuscript.

Flow Cytometry

Plots

Confirm that:

- The axis labels state the marker and fluorochrome used (e.g. CD4-FITC).
- The axis scales are clearly visible. Include numbers along axes only for bottom left plot of group (a 'group' is an analysis of identical markers).
- All plots are contour plots with outliers or pseudocolor plots.
- A numerical value for number of cells or percentage (with statistics) is provided.

Methodology

Sample preparation	As described in the Methods section. Briefly, the single nuclei were isolated by mechanical homogenisation and washed. The nuclei were stained with commercially available Hoechst 33342 dye (NucBlue , R376050). The samples were kept on ice and directly loaded onto the FACS-sorter.
Instrument	Becton Dickinson (BD) Influx, XDP, or FACSAria
Software	Proprietary software of the selected sorter.
Cell population abundance	N/A
Gating strategy	Single nuclei were selected for single signal on the SCC and FCC to avoid aggregates. The Hoechst-positive nuclei were selected without any size limit. The gating strategy is available as Supplementary Figure 1.

- Tick this box to confirm that a figure exemplifying the gating strategy is provided in the Supplementary Information.